

CZECH TECHNICAL UNIVERSITY IN  
PRAGUE

Faculty of Nuclear Sciences and Physical  
Engineering

Department of Physics



## Bachelor thesis

Measurement of charged particle spectra at the  
LHC at 13 TeV

**Filip Nechanský**

Supervisor: Mgr. Oldřich Kepka, Ph.D.

Prague, 2015

ČESKÉ VYSOKÉ UČENÍ TECHNICKÉ  
V PRAZE

Fakulta Jaderná a Fyzikálně Inženýrská

Katedra Fyziky



## Bakalářská práce

Měření spekter nabitých částic na LHC při  
těžištové energii 13TeV

**Filip Nechanský**

Supervisor: Mgr. Oldřich Kepka, Ph.D.

**Praha, 2015**



*Katedra:* fyziky

*Akademický rok:* 2014/15

## ZADÁNÍ BAKALÁŘSKÉ PRÁCE

*Posluchač:* Filip Nechanský

*Obor:* Experimentální jaderná a částicová fyzika

*Název práce:* Měření spekter nabitých částic na LHC při těžišťové energii 13TeV

*Název práce:* Measurement of charged particle spectra at the LHC at 13TeV  
(anglicky)

*Osnova:*

1. Seznamte se s principem měření spekter nabitých částic vnitřním detektorem ATLAS v událostech minimum bias.
2. Diskutujte způsob rekonstrukce nabitých drah vnitřním detektorem ATLAS.
3. Napište program, který, z dodaných buď experimentálních nebo simulovaných ATLAS dat, vybere zajímavé případy a spočítá relevantní spektra nabitých částic.
4. Svoje výsledky diskutujte v bakalářské práci a zasad'te je do kontextu již provedených minimum bias měření.

*Doporučená literatura:*

- [1] Charged-particle multiplicities in pp interactions measured with the ATLAS detector at the LHC, New J. Phys. 13:053033, 2011, časopis New Journal of Physics, <http://arxiv.org/abs/1012.5104>.
- [2] Sjostrand T., Corke R., Multiparton Interactions with an x-dependent Proton Size, JHEP 05 (2011) 009, časopis Journal of High Energy Physics, <http://arxiv.org/abs/1101.5953>.
- [3] Cornelissen T., Elsing M., Fleischmann S., Liebig W., Moyse E., Salzburger A., Concepts, Design and Implementation of the ATLAS New Tracking (NEWT), ATL-SOFT-PUB-2007-007, ATLAS dokument, 2007, <http://cds.cern.ch/record/1020106>.

*Jméno a pracoviště vedoucího bakalářské práce:*

Mgr. Oldřich Kepka, Ph.D., Fyzikální ústav, AV ČR, v.v.i.

Do bakalářské práce se vkládá zadání a dále na stranu předcházející obsahu abstrakt a klíčová slova. Součástí zadání bakalářské práce je její uložení na webové stránky katedry fyziky a zaslání abstraktu a klíčových slov ve formátu WORD na e-mailovou adresu katedry fyziky: [kf@fjfi.cvut.cz](mailto:kf@fjfi.cvut.cz)

*Datum zadání bakalářské práce:* 16.10.2014

*Termín odevzdání bakalářské práce:* 07.07.2015

  
.....  
Vedoucí katedry

  
.....  
Děkan

*V Praze dne* 16.10.2014

**Prohlášení:**

Prohlašuji, že jsem svou bakalářskou práci vypracoval samostatně a použil jsem pouze podklady (literaturu, software, atd.) uvedené v příloženém seznamu.

Nemám závažný důvod proti užití tohoto školního díla ve smyslu §60 Zákona .121/2000 Sb., o právu autorském, o právech souvisejících s právem autorským a o změně některých zákonů (autorský zákon).

V Praze dne

*Title:*

**Measurement of charged particle spectra at the LHC at 13 TeV**

*Author:* Filip Nechanský

*Specialization:* Experimental nuclear and particle physics

*Sort of project:* Bachelor thesis

*Supervisor:* Mgr. Oldřich Kepka, Ph.D.

---

*Abstract:* The measurement of charged particle spectra is performed for centre-of-mass energy  $\sqrt{s} = 13$  TeV in experiment ATLAS. It is an inclusive measurement aiming at fast comparison of particle activity between data and theoretical model. Data are acquired with minimal model dependence avoiding unnecessary bias. Various efficiencies and fractions are determined in order to correct reconstructed spectra of tracks in the Inner Detector to distributions of primary particles. Correction of certain distributions involves more sophisticated methods, such as Bayesian unfolding. The corrected distributions are compared to Monte Carlo generators - Pythia 8 (A2 and Monash tunes), Herwig++, EPOS and QGSJET. Though no generator describes measured data perfectly, in many cases the differences are within few percent. The measured average number of charged particles per unit of pseudorapidity is  $2.876 \pm 0.001922(stat.) \pm 0.03526(syst.)$  and is found to be in a good agreement with EPOS generator. Apart from the analysis, an introduction to simulation of proton-proton collision is given in this thesis. Furthermore, the detector ATLAS is described, as well as methods of track reconstruction.

*Key words:* Minimum Bias, charged particle spectra, ATLAS, reconstruction of particles, data correction

*Název práce:*

## **Měření spekter nabitých částic na LHC při těžiškové energii 13TeV**

*Autor:* Filip Nechanský

*Abstrakt:* Měření spekter nabitých částic je provedeno při těžiškové energii  $\sqrt{s} = 13$  TeV na experimentu ATLAS. Je to inkluzivní měření zaměřené na rychlé porovnání částicové aktivity mezi daty a teoretickými modely. Data jsou získána s minimální modelovou závislostí, aby se snížili zbytečné vlivy. Jsou určeny různé efektivity a frakce, aby bylo možné opravit rekonstruovaná spektra drah ve vnitřním detektoru na distribuce nabitých částic. Korekce některých distribucí zahrnují více sofistikované metody, jako je Bayesian unfolding. Opravené distribuce jsou porovnány s Monte Carlo generátory - Pythia 8 (verze A2 a Monash), Herwig++, EPOS a QGSJET. I když žádný generátor nepopisuje naměřená data přesně, v mnoha případech je rozdíl v rámci několika procent. Naměřený průměrný počet částic na jednotku pseudorapidity je přibližně  $2.876 \pm 0.001922(stat.) \pm 0.03526(syst.)$  a je v dobré shodě s generátorem EPOS. Kromě analýzy je v této práci uveden úvod do simulací proton-protonových srážek. Dále je popsán detektor ATLAS, stejně jako metody rekonstrukce drah.

*Klíčová slova:* Minimum Bias, spektra nabitých částic, ATLAS, rekonstrukce částic, korekce dat

## **Acknowledgement**

First, I would like to thank my supervisor Oldřich Kepka, who was able to teach me more in one year than I ever imagined. I am thankful for the time he invested and patience he had with me. I am also grateful to whole Minimum Bias 13TeV group in ATLAS and especially to Thorsten Kühl, who encouraged my work there. Finally, I would like to thank all the others, who supported my work on this thesis, most importantly my family.

# Contents

<b>Introduction</b>	<b>12</b>
<b>1 Theoretical overview</b>	<b>13</b>
1.1 Quantum Chromodynamics . . . . .	13
1.1.1 Hard processes . . . . .	14
1.2 Parton Showers . . . . .	15
1.2.1 Initial state radiation . . . . .	16
1.3 Multiparton interactions . . . . .	17
1.4 Hadronization . . . . .	18
1.5 Overview of generators . . . . .	19
<b>2 Experiment ATLAS</b>	<b>20</b>
2.1 Large Hadron Collider . . . . .	20
2.2 ATLAS detector overview . . . . .	20
2.2.1 ATLAS triggers . . . . .	21
2.3 Inner detector . . . . .	22
2.3.1 Pixel detector . . . . .	23
2.3.2 Insertable Beam Layer . . . . .	24
2.3.3 SCT detector . . . . .	24
2.3.4 TRT detector . . . . .	24
2.4 Calorimeters and muon spectrometer . . . . .	25
<b>3 Tracking</b>	<b>26</b>
3.1 Tracking algorithms . . . . .	26
3.1.1 Inside-out algorithm . . . . .	26
3.1.2 Outside-in algorithm . . . . .	27
3.2 Vertex reconstruction . . . . .	27
<b>4 Strategy behind current measurement</b>	<b>28</b>
4.1 Clasification of tracks and vertices . . . . .	28
4.2 Selections . . . . .	28
4.2.1 Event selection . . . . .	28
4.2.2 Track selection . . . . .	29
4.3 Background . . . . .	30
4.3.1 Background to primary particles . . . . .	30
4.4 Weight corrections . . . . .	30

<b>5</b>	<b>Tracking and vertexing efficiencies</b>	<b>32</b>
5.1	Vertex reconstruction efficiency . . . . .	32
5.1.1	Vertex efficiency vs. $n_{sel}^{BL}$ . . . . .	32
5.1.2	Vertex efficiency vs. $\Delta z_0$ for $n_{sel}^{BL} = 2$ . . . . .	32
5.1.3	Vertex efficiency vs. $\eta$ for $n_{sel}^{BL} = 1$ . . . . .	34
5.2	Tracking efficiency . . . . .	34
5.2.1	Matching reconstructed and truth particle . . . . .	35
5.2.2	Tracking efficiency vs $p_T$ and $\eta$ . . . . .	35
5.3	Secondary particles . . . . .	36
5.4	Tracks migrating to kinematic region . . . . .	36
<b>6</b>	<b>Corrections</b>	<b>38</b>
6.1	Unfolding . . . . .	38
6.1.1	Bayesian unfolding . . . . .	38
6.2	Correction to $\frac{1}{N_{ev}} \frac{dN_{ev}}{dn_{ch}}$ . . . . .	39
6.3	Correction to mean $p_T$ vs $n_{ch}$ . . . . .	39
6.4	Corrections to $\frac{1}{N_{ev}} \frac{dN_{ch}}{d\eta}$ and $\frac{1}{N_{ev}} \frac{1}{2\pi p_T} \frac{d^2 N_{ch}}{d\eta dp_T}$ distributions . . . . .	41
<b>7</b>	<b>Analysis of 13 TeV data</b>	<b>43</b>
7.1	13 TeV data . . . . .	43
7.2	Re-weighting of the Monte Carlo . . . . .	43
7.3	Raw distributions . . . . .	44
7.4	Systematic and statistical errors . . . . .	45
7.5	Final results . . . . .	46
	<b>Summary</b>	<b>48</b>
	<b>Appendix A</b>	<b>49</b>

# List of Figures

1.1	Dependence of coupling constant of strong interaction on $Q^2$ . Taken from [2]. . . . .	14
1.2	Example of parton distribution function of a proton. . . . .	15
1.3	Example of gluon emission. . . . .	15
1.4	(a) Comparison of particle multiplicities, (b) cross-section of inclusive jet production. . .	17
1.5	Illustrations for string model of hadronization. . . . .	18
2.1	Overview of main parts of ATLAS. . . . .	21
2.2	Overview of Inner Detector. . . . .	22
2.3	Definition of impact parameters $d_0$ and $z_0$ , taken from [13]. . . . .	23
2.4	Distribution of hits vs. $\eta$ for (a) Pixel and (b)SCT detector. . . . .	23
2.5	Possible strip detector configurations. . . . .	24
3.1	Illustration showing roughly process of inside-out tracking. . . . .	27
4.1	Picture of possible process leading to higher reconstructed momentum. . . . .	29
4.2	Distribution of primary particles and secondaries. . . . .	31
5.1	Vertex efficiency vs. $n_{sel}^{BL}$ . . . . .	33
5.2	Correlation between $n_{sel}^{BL}$ of two phase space regions. . . . .	33
5.3	Vertex efficiencies for lowest $n_s el^{BS}$ bins in given phase-space. . . . .	34
5.4	Tracking efficiency vs. (a) $p_T$ and (b) $\eta$ . . . . .	35
5.5	Tracking efficiency in $p_t$ vs. $\eta$ . . . . .	36
5.6	Fraction of secondary particles vs. (a) $p_T$ and (b) $\eta$ . . . . .	37
5.7	Fraction of (a) electrons, (b) non-electrons and (c) secondary particles in general. . . . .	37
5.8	Fraction of tracks which migrated outside of the kinematic region. . . . .	37
6.1	Effects of corrections on the distribution of events vs. $n_{ch}$ . . . . .	40
6.2	Effects of corrections on (a) sum of $p_T$ and (b) sum of tracks and (c) mean $p_T$ . . . . .	40
6.3	Effects of corrections on the $\eta$ distribution. . . . .	41
6.4	Effects of various steps of corrections on the $p_T$ distributions. . . . .	42
6.5	Effect of iterative unfolding on $p_T$ distribution. . . . .	42
7.1	Distribution of vertices as function of $z$ and $z$ -weight. . . . .	44
7.2	Raw distributions for data and Pythia8 A2 normalized to 1 . . . . .	44
7.3	Comparison of systematic distributions and of the errors for the $p_T$ . . . . .	45
7.4	Corrected data and various Monte Carlo for densities vs. $p_T$ and $\eta$ . . . . .	47
7.5	Corrected data and various Monte Carlo for event density and $\langle p_T \rangle$ vs. $n_{ch}$ . . . . .	47
7.6	Raw distributions for data and Pythia 8 A2 normalized by number of events. . . . .	49

# Introduction

Main focus of modern particle physics is to study a borderline science, e.g. search for Higgs boson or Quark Gluon Plasma. However, many other studies are necessary to make those studies possible. Many processes studied have a small cross-section and require precise description of the final states - and the simulation of the final states requires good modeling of  $pp$  collision. Furthermore, one must take into consideration effects of the detector, background and other interfering effects. Analyses focused on basic properties of  $pp$  collisions have therefore the highest priority in first weeks of gathering data.

The measurement of charged particle spectra is one of those basic studies. It focuses on wide range of issues, as e.g. tracking, vertexing and is the most inclusive  $pp$  measurement from the trigger point of view. Similar measurements were or are done in ATLAS for all center-of-mass energies of LHC. For  $\sqrt{s} = 0.9, 2.36, 7$  TeV they are summarized in the article “Charged-particle multiplicities in  $pp$  interactions with ATLAS detector at the LHC” [1], which also serves as a basis of this thesis. Analysis of 8 TeV data is in progress, but the code was available and served as inspiration for this analysis.

Particle production at low momentum cannot be directly calculated and there are many Monte Carlo generators (MC), with many free parameters, predicting structure of the collisions. Their results can vary significantly<sup>1</sup> and for this reason they must be compared with data and then tuned accordingly. Minimal event selection is applied in order to minimize model dependence and other biases - for this reason such measurement is often called Minimum Bias measurement.

There are four main distributions studied:

$$\frac{1}{N_{ev}} \frac{dN_{ch}}{d\eta}, \quad \frac{1}{N_{ev}} \frac{1}{2\pi p_T} \frac{d^2 N_{ch}}{d\eta dp_T}, \quad \frac{1}{N_{ev}} \frac{dN_{ev}}{dn_{ch}}, \quad \langle p_T \rangle \text{ vs. } n_{ch}. \quad (1)$$

The first two are densities of particles as function of  $\eta$  and  $p_T$ . The third shows distribution of events per number of charged particles. This number will be further denoted as  $n_{ch}$ . The last observable is the average  $p_T$  for given  $n_{ch}$ .  $N_{ev}$  stands for number of events within studied selection.

The measurement is done for primary particles, which were in previous analyses defined as follows: Charged particles with a mean lifetime  $\tau > 0.3 \cdot 10^{-10}$  s either directly produced in  $pp$  interactions or from subsequent decay of particles with a shorter lifetime [1, Page 3]. Current definition has one more requirement: strange baryons, such as  $\Sigma^\pm$  or  $\Omega$ , are not included in primary particles. This is because they have low chance to be reconstructed and keeping them in the definition would introduce a Monte Carlo dependence, which is something undesirable in Minimum Bias analysis and makes it impossible to determine model-independent tracking efficiency.

Part of this measurement consists of the estimation of secondary particles, background and pile-up. Great focus is also put on the determination of efficiencies for tracks, triggers or events, which will be thoroughly discussed in chapter 5.

---

<sup>1</sup>Which will be demonstrated in results.

# Chapter 1

## Theoretical overview

Description of a collision of particles is a difficult task. Theories such as Quantum Chromodynamics (further QCD) may in principle yield precise results, when perturbation theory with many orders is used. But description of process as complicated as collision of two protons with both hard and soft processes is nearly impossible using the perturbative framework. Various models and tricks are therefore used to get accurate results. This whole chapter is based on references [2, 3, 4].

Simulation of a  $pp$  collision goes approximately through the following steps: We start with a collision of 2 partons - hard process of interest (e.g  $ug \rightarrow ug$ ) - and its cross-section. Next, decays of short lived particles ( $t, W, Z$ ) must be evaluated. However, a collision of particles gives rise to accelerated coloured particles, which leads to bremsstrahlung, emissions of additional particles. This is called a parton shower and it can be also viewed as addition of other orders of perturbation.

Next part to consider is that hadron is made of large number of partons, therefore multiple parton-parton interactions in single collision are possible and must be included. All those collisions also have their own parton showers. Now, when we have a description of a parton-level of a collision, hadronization takes place. Last step in the simulation is to decay the unstable short-living hadrons.

The most important steps will be described in following sections, starting with short overview of QCD.

### 1.1 Quantum Chromodynamics

Quantum Chromodynamics is the theory of strong interaction - interaction between quarks and gluons. Quarks are fermions, are denoted as  $q$  and have six flavours (types)  $u, d, s, c, b, t$ , where for example two  $u$  (up) and one  $d$  (down) quarks constitute a proton<sup>1</sup>. Together with the theory of electroweak interaction, strong interaction is part of Standard Model of physics and therefore basis of modern particle physics.

Similarly to electrodynamics, strong interaction has a charge. More precisely it has three charges, called colours: red and anti-red ( $R\bar{R}$ ), green and anti-green ( $G\bar{G}$ ), and blue and anti-blue ( $B\bar{B}$ ). Colour was first implemented as another degree of freedom, since  $\Delta^{++}$  would have a symmetrical wave function even though it is a fermion. The number of colours was definitely determined from the ratio of cross-section of  $e^+e^- \rightarrow q\bar{q}$  and  $e^+e^- \rightarrow \mu^+\mu^-$  processes.

Lagrangian of QCD is based on SU(3) group<sup>2</sup>. Its 9 linearly independent elements can be divided between one singlet  $\frac{1}{\sqrt{3}}(R\bar{R} + G\bar{G} + B\bar{B})$  invariant under SU(3) transformation and eight elements affected by such transformation. For this reason QCD has 8 generators - gluons - as carriers of the interactions. Unlike photons, gluon carry charge and therefore can emit additional gluons. This small detail has large consequences and it is the main reason why strong interaction is stronger at larger

---

<sup>1</sup>This is not entirely true since sea of virtual particles is also present.

<sup>2</sup>Unitary 3x3 matrices with determinant equal to 1.

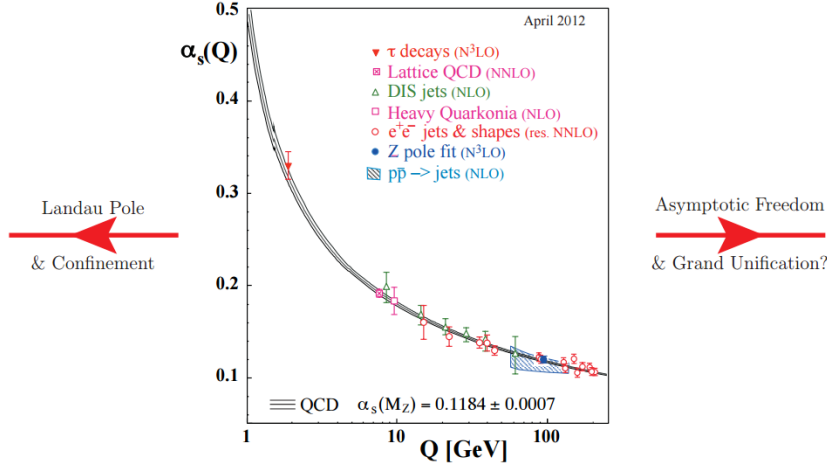


Figure 1.1: Dependence of coupling constant of strong interaction on  $Q^2$ . Taken from [2].

distances. QCD is not scale-independent and coupling constant of strong interaction  $\alpha_s$  is dependent on  $Q^2$  similarly to electromagnetic interaction.

Nevertheless, here the similarity ends, since the dependence on the momentum transfer is opposite. QCD is strongest at low  $Q^2$  as can be seen in Figure 1.1. This fact leads to confinement - quarks are confined in baryons and mesons as colour singlets. For this reason colour cannot be seen directly in low energy experiments. On the other hand, when energy is high, force acting on quarks is weaker and they can move as if they were free. This is called asymptotic freedom. At energies around  $10^{15} - 10^{17}$  GeV the strong interaction is as weak as the electromagnetic interaction. The fact that coupling constant can have low values enables usage of perturbative quantum field theory.

### 1.1.1 Hard processes

First step of the simulation of  $pp$  collision is to get probability of hard process of interest, since it can be acquired by perturbative calculation. Thus we get cross-section  $\sigma_{ab \rightarrow n}$ . In reality we however collide compound particles and therefore the cross-section  $\sigma$  of a process  $a + b \rightarrow n$  must be rewritten as

$$\sigma = \int dx_a dx_b f_a^1(x_a, Q^2) f_b^2(x_b, Q^2) d\sigma_{ab \rightarrow n}, \quad (1.1)$$

where  $Q^2$  is momentum transfer squared, which defines scale of our interaction, and  $f_i^k$  is parton distribution function (PDF) of parton  $i$  to be found in particle  $k$ , which is in our case proton.  $x_i$  is fraction momentum of proton carried by parton  $i$ . The possibility to write down the total cross-section as a convolution of matrix element and parton distribution function is called factorization and was proven theoretically for inclusive observables.

Parton distribution function describes, as one would expect, probability distribution of partons carrying fraction  $x$  of momentum in given particle. If we take for example proton, then in first approximation one would get distribution of quarks  $u, u, d$ . In reality, however, protons are active soup of partons: quark anti-quark pairs appearing from vacuum or gluons, which create so-called sea of particles inside the particle. In the first approximation of QCD, the distribution of particles would be independent of a scale ( $Q^2$ ), this fact is called Bjorken scaling. However this is not the case and as a result, distribution is affected by the scale. The proton distribution function is shown for values of  $Q^2 = 10 \text{ GeV}^2$  and  $Q^2 = 10000 \text{ GeV}^2$  in Figure 1.2. There is for example larger fraction of low  $x$  gluons and sea particles in case of the higher  $Q^2$  coming from a parton splittering (e.g.  $q \rightarrow qg$ ).

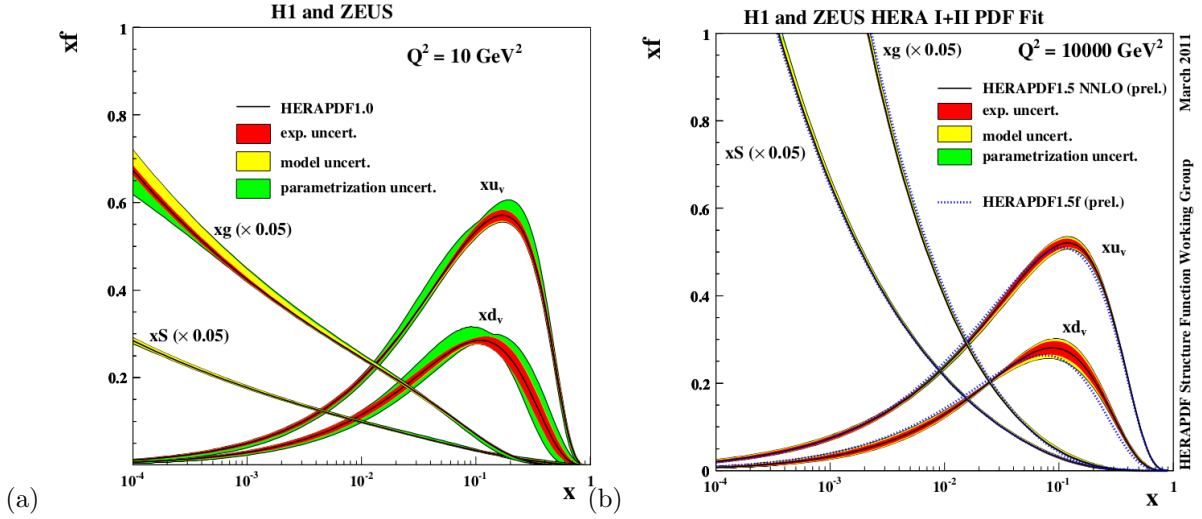


Figure 1.2: Example of parton distribution function of a proton, including  $u$  and  $d$  quarks, gluons and sea of particles, as function of fraction of momentum  $x$  of the proton. Shown for (a)  $Q^2 = 10 \text{ GeV}$  and (b)  $Q^2 = 10000 \text{ GeV}$ . Taken from [5].

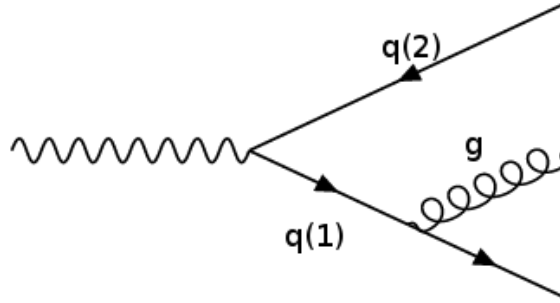


Figure 1.3: Example of emission of gluon by one of quarks after hard process.

Large number of hard processes must be available in Monte Carlo generators in order to study processes with low cross-section. However those are usually only first or next order calculations, other orders are simulated approximately through e.g. parton showers.

## 1.2 Parton Showers

As in the case of electromagnetism, also in QCD moving charge (colour) in a field results in a emission of particles. This principle is used to add additional emissions to hard process. Consider that we want to expand the original hard process  $x \rightarrow q\bar{q}$ , where  $x$  can be photon, with additional emission of gluon  $g$  by one of the quarks to get process  $x \rightarrow q\bar{q}g$ . Cross-section of one such process, displayed in Figure 1.3, can be written as:

$$dP = \frac{d\sigma_{q\bar{q}g}}{\sigma_{q\bar{q}}} = \frac{\alpha_s}{2\pi} \frac{4}{3} \frac{x_1^2 + x_2^2}{(1-x_1)(1-x_2)} dx_1 dx_2 \approx \frac{\alpha_s}{2\pi} \frac{4}{3} \frac{dQ^2}{Q^2} \frac{1+z^2}{1-z} dz. \quad (1.2)$$

$x_i$  is fraction of energy of quark  $q(i)$ :  $x_i = 2E_i/E_{cm}$ , where  $E_i$  is energy of corresponding quark and  $E_{cm}$  is center-of-mass energy.  $Q^2$  is virtuality<sup>3</sup> of the quark  $q(1)$  and  $z$  is a fraction of its original energy and energy the quark has after the gluon emission. Obviously,  $1 - z$  refers to fraction of that energy carried by the gluon.

The divergence for  $Q^2 \rightarrow 0$  is called "collinear" singularity, meaning that the gluon is emitted in the direction of the quark. In proper QCD derivation it can be demonstrated that divergence of such emission together with divergence of other processes, e.g. emission of gluon by one quark and capture by the other, gives finite value of the cross-section. However, parton shower consists only of tree level diagrams. In order to have a finite prediction, a cut on  $Q^2$ , motivated by the complete calculation, is implemented and it is found to be around 1 GeV. Second singularity is when  $1 - z \rightarrow 0$ . This is called soft-gluon singularity, since gluon carries only small energy.

Advantage of equation (1.2) is that it can be generalized to multiple emissions and it also shows, that this event can be separated into the hard process followed by gluon emission. Thus we get generalized formulas called DGLAP equations [3]:

$$dP_{a \rightarrow bc} = \frac{\alpha_s}{2\pi} \frac{dQ^2}{Q^2} F_{a \rightarrow bc}(z) dz, \quad (1.3)$$

where  $F_{a \rightarrow bc}(z)$  in case of  $q \rightarrow gq$  is  $\frac{4}{3} \frac{1+z^2}{1-z}$ , for process  $g \rightarrow gg$  it takes form  $3 \frac{(1-z(1-z))^2}{z(1-z)}$ . This way we can get differential cross-section of process of interest, where dependence on  $Q^2$  is therefore only in factor  $dQ^2/Q^2$  and type of emission is dependent only on  $z$  and is characterized by function  $F_{a \rightarrow bc}(z)$  called kernel.

Still, we can see that cross-section of our new process may exceed that of the basic hard process. This is solved by normalizing the probability of emission (of one or more particles), which gets us the final form of the equation:

$$dP_{a \rightarrow bc} = \frac{\alpha_s}{2\pi} \frac{dQ^2}{Q^2} F_{a \rightarrow bc}(z) dz \exp \left( - \sum_{a,b} \int_{Q^2}^{Q_{max}^2} \frac{dQ'^2}{Q'^2} \int \frac{\alpha_s}{2\pi} P_{a \rightarrow bc}(z') dz' \right), \quad (1.4)$$

where expression in the exponent is called Sudakov factor. This ensures that total probability never exceeds unity.

Now, when we have a way to add emissions to original cross-section, we may extend this idea. By iterative process, cascade of those emissions can create shower of particles, to which we refer as parton shower. It should be noted, that not only the original quarks, but also produced gluons can radiate.

When this emission takes place after the hard process, then it is called final state radiation (FSR). It is simulated with decreasing virtuality, starting with highest value at hard process and then slowly decreasing to the  $Q^2$  cut-off state by emission of gluons.

### 1.2.1 Initial state radiation

Interacting quark can also emit particle before the hard process. As it approaches the interaction point, it "gains" space-like virtuality by emission of quons. This is called initial state radiation (ISR) and on first look it is very similar to FSR. It is however slightly more complicated, since the structure of colliding protons must be taken into account.

One approach to handle the ISR could be to take a quark from the distribution function and evolve it in a way similar to the FSR. If resulting quark does not match criteria for the hard process, nothing happens (all emitted gluons collapse back to the quark) and event is discarded. Otherwise is the event kept and extended by FSR. This method is called forward evolution and because vast majority of events is discarded, it is not a practical approach to do the ISR.

<sup>3</sup>Virtuality is an absolute value of four-momentum  $P$  of particle squared:  $Q^2 = |P^2|$ . More off-shell this value is, more virtual given particle is. It can be either time-like virtuality for  $P^2 > m^2 \approx 0$  or space-like for  $P^2 < m^2 \approx 0$ .

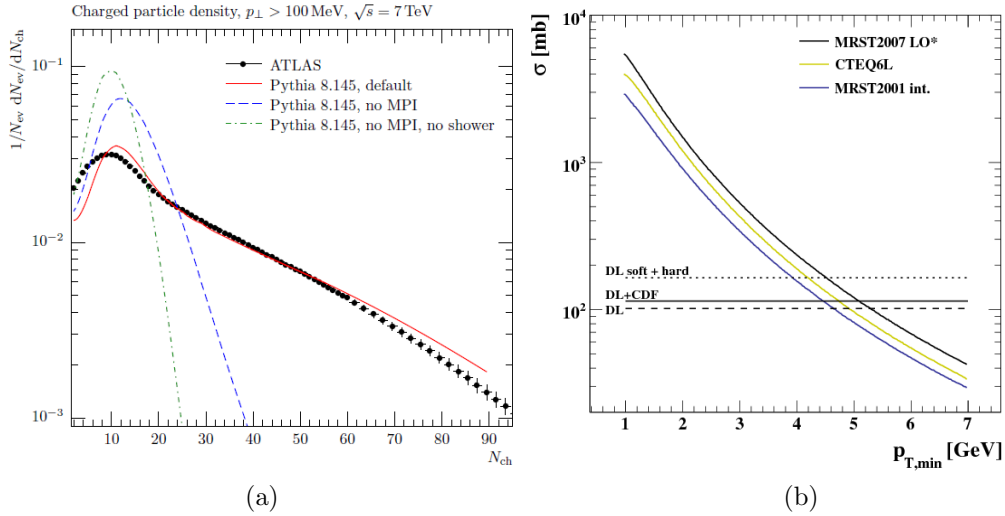


Figure 1.4: (a) Comparison of charged-particle multiplicities between ATLAS data and Pythia models with and without parton showers and MPI, taken from [4]. (b) cross-section of inclusive jet production for several PDFs plotted with total  $pp$  cross-section, taken from [4].

Second and more useful way is to take hard process with a given quark configuration and evolve it backwards. Basically we ask, what is the probability that a given state of quark  $b$  came from process  $a \rightarrow bc$ , moving again from highest virtuality at the hard process to lowest virtuality at the proton. At the end, we can take the distribution function to see how probable it is to find a quark with such properties. As in case of FSR,  $Q^2$  cut-off and Sudakov factor is used to normalize probability.

Effect of parton showers on a minimum bias charged particle multiplicity can be seen of Figure 1.4(a). It widens the charged particle density, but still there is enormous difference between the simulation and data.

### 1.3 Multiparton interactions

At this point hard process and corresponding parton showers are created. As was mentioned earlier, one of the complications of proton-protons interaction is that proton is a compound particle and therefore more than one parton per proton may collide. This is apparent from previously mentioned Figure 1.4, where only after inclusion of multiparton interactions (MPI) the model describes the data with some accuracy.

First model of MPI was created by Sjostrand and van Zijl [4]. Parton-parton interaction has largest contribution in t-channel, which has cross-section proportional to  $dp_T^2/p_T^4$ . If we integrate from  $p_{T,min}$  to infinity and also include the parton densities, we get integrated cross-section shown in Figure 1.4(b). At some point the integrated cross-section  $\sigma_{int}$  exceeds the total cross-section of  $pp$  collision  $\sigma_{tot}$ . Furthermore, it diverges for  $p_{T,min} \rightarrow 0$ , which presents a problem.

In order to solve this, one must realize that one can have more parton-parton interactions. Their cross-section is summed and gives the integrated cross-section. Thus can be both cross-sections connected through simple formula  $\sigma_{int} = \langle n \rangle \cdot \sigma_{tot}$ , where  $\langle n \rangle$  is the average number of interactions and depends on  $p_{T,min}$ . Poisson distribution can be then used to estimate number of parton-parton interactions in given collision. Nevertheless, this explanation does not really solve our problem, since it would imply infinite number of interactions for  $p_{T,min} \rightarrow 0$ .

In order to resolve the divergence, colour screening is introduced. When a particle has really small

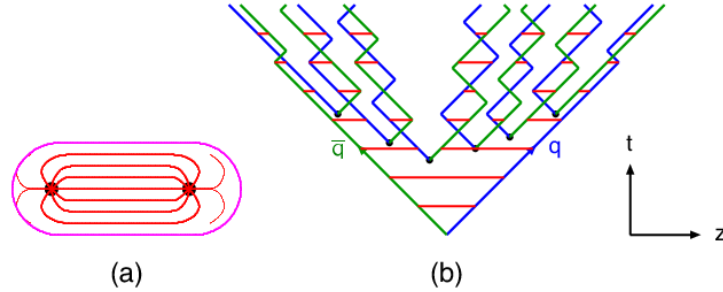


Figure 1.5: (a) Illustration of colour flux tube between two particles in string model for hadronization. (b) Illustration of gradual breaking of string between two quarks. Taken from [4].

momentum, its wavelength is comparable to the size of the proton and it interacts not only with the closest partons, but feels the colour charge of the proton as a whole. This effectively introduces a lower cut-off on  $p_T$ , which is found to be around 2 GeV. It is one of the parameters, which are tuned when comparing simulation with data.

Furthermore, it is expectable that when protons collide with smaller impact parameter, more partons will interact. Dependency of  $\langle n \rangle$  on impact parameter  $b$  is therefore the last detail which needs to be added to a proper MPI model. The dependence is found to be  $\langle n \rangle = k \cdot O(b)$ , where  $k$  is constant determined from data and  $O(b)$  is overlap function derived as convolution of two Gaussian functions.

## 1.4 Hadronization

At this point, parton level of the collision is described. Last necessary step in the model is hadronization of particles. Resulting hadrons can be either measured directly or decay into another hadrons which we are able to detect.

Process of hadronization is not well understood. There are some rigorous approaches to this problem, but those are only for case of non-relativistic processes, which is not sufficient since we collide particles with energy in orders of TeV. For this reason, several models are used to describe hadronization process. Here, only two will be mentioned: string and cluster model.

The idea behind the string model is that partons with opposite colour charge are connected through colour flux tube, as illustrated in Figure 1.5(a). Such string has an energy density, which is in QCD found to be constant and therefore coupling energy of two quarks is proportional to the distance between them, with value of around 1 GeV/fm. As quarks move away from each other, energy is cumulated and when it is high enough, it is favourable to create  $q\bar{q}$  pair and break the string. This usually happens when quarks are separated by distance of 1-5 fm. After few successive break-ups we get relatively stable state, with one obvious restriction, that the resulting hadrons must have on-shell mass. Illustration of such cascade is in Figure 1.5(b).

String model has great predictive power, however its disadvantage is that it has many parameters, which have to be derived from data. Cluster model originally did not have this drawback. Its basic idea is again to make  $q\bar{q}'$  colour singlets based on colour flow in the event. Those pairs are the constituents of the cluster, which is characterized only by its mass and colour composition and any internal structure is omitted. Through successive decay, mass of heavier clusters is lowered until some conditions are satisfied. Thus we get intermediate state of clusters, which are then hadronized into the hadrons.

Even though the initial cluster model had less parameters, over time it had to be adjusted and modified and in the end one ends up with similar number of parameters as in the string model.

## 1.5 Overview of generators

Several Monte Carlo generators are used throughout the analysis. Either they were used to prepare analysis and estimate some results, or they are compared to the data, to give us an idea about how well are we able to describe the collisions. Those generators will be further tuned using the new data for  $\sqrt{s} = 13$  TeV. Three main generators used are: PYTHIA 8, HERWIG++ and EPOS.

The **Pythia 8** uses parton showers (both FSR and ISR), MPI and the string hadronization model. Two tunes were used, both tuned using 7 TeV data. A2, the ATLAS minimum-bias tune, should be able to describe minimum bias events and Monash, which aside from ATLAS data uses also results from SPS and Tevatron and is constructed to predict better underlying event observables<sup>4</sup> [6].

The **Herwig++** also includes parton showers, though they are order differently. It has implemented the cluster hadronization model and MPI with energy dependent  $p_T$  cut-off [6]. Finally, the **EPOS** uses completely different approach, using Gribov-Regge theory - a field theory similar to QCD, but containing also soft scattering and using hydrodynamical approach as used in a heavy ions collision physics. Unlike the Pythia and Herwig it doesn't use standard parton distribution functions [7].

Another generator, **QGSJET**, will be showed in final result. It is also based on Gribov-Regge theory and is designed to describe cosmic rays.

The Pythia 8 A2 will appear more frequently, since it was used to derived e.g. tracking efficiency and it is our default generator to compare to data. Sometimes postfix ND will be added to the name of generator, which refers to non-diffractive part of spectrum, which consists of events, where both protons survived the collision, though additional particles were emitted. These account for most majority of events. Other parts of spectra are single-diffractive (SD) and double-diffractive (DD). However description of diffraction is beyond the scope of this thesis and is not necessary for the analysis.

---

<sup>4</sup>Underlying event is a mix of soft and hard processes accompanying event of study, such as jet production.

## Chapter 2

# Experiment ATLAS

This chapter describes the experiment ATLAS, in which this measurement takes place, starting with description of the Large Hadron Collider, which supplies ATLAS with collisions, and ending with description of individual sub-detectors.

### 2.1 Large Hadron Collider

Large Hadron Collider (LHC) is a circular proton-proton collider situated at CERN near Geneva, Switzerland. It collides protons with the largest center-of-mass energy in the world, with maximal planned energy of 14 TeV and current energy of 13 TeV. High energies enable to study problems on and beyond borders of modern science. For example in year 2012 both ATLAS and CMS, the general purpose experiments of the LHC, were able to confirm Higgs boson, missing particle of the Standard Model [8]. Experiment ALICE on the other hand studies e.g. Quark Gluon Plasma, theorized state of matter present at earliest moments of the universe. The last experiment, LHCb, focuses on the study of b-hadrons.

Tunnel of the LHC is around 27 km long, with additional smaller accelerators providing injecting energy of 900 GeV. There are approximately 2800 bunches at the same time along the ring, with approximately  $10^{11}$  protons present in each bunch. Bunches flow through two separate magnetic channels, which only intersect in four places, where the four experiments are situated. Magnets need to be cooled down to  $-271.3^{\circ}\text{C}$ , which is ensured by large amount of liquid helium. In order to minimize loss of particles, ultra-high vacuum must be created in tubes with the beam particles. The protons currently collide  $25 \cdot 10^6$  times per second with planned frequency  $40 \cdot 10^6$  times per second in the summer 2015. Number of colliding particles and frequency of their collision can be summed in luminosity, which is a proportionality factor between cross-section of some process and number of events in which this process occurred.

### 2.2 ATLAS detector overview

ATLAS, A Toroidal LHC Apparatus, is a cylindrical detector consisting of main barrel and two discs (end-caps). It is 42 m long, has diameter of 22 meters and weights around 7000 tons. The detector consists of four main parts - Inner Detector, electromagnetic calorimeter, hadronic calorimeter and muon spectrometer. The Inner Detector is surrounded by 2T solenoid superconducting magnet, with additional eight 0.5T super-conducting toroidal magnets placed symmetrically around the beam pipe and two additional 1T in the end-caps. Schematic view of the detector is in Figure (2.1).

Coordinates on the ATLAS are defined as follows: origin point is in the center of the detector with  $z$  axis parallel with the beam pipe.  $x$  coordinate points directly to the center of the LHC ring and  $y$  is perpendicular to both  $x, z$  and points upwards. However, the  $x, y, z$  coordinates are not commonly used

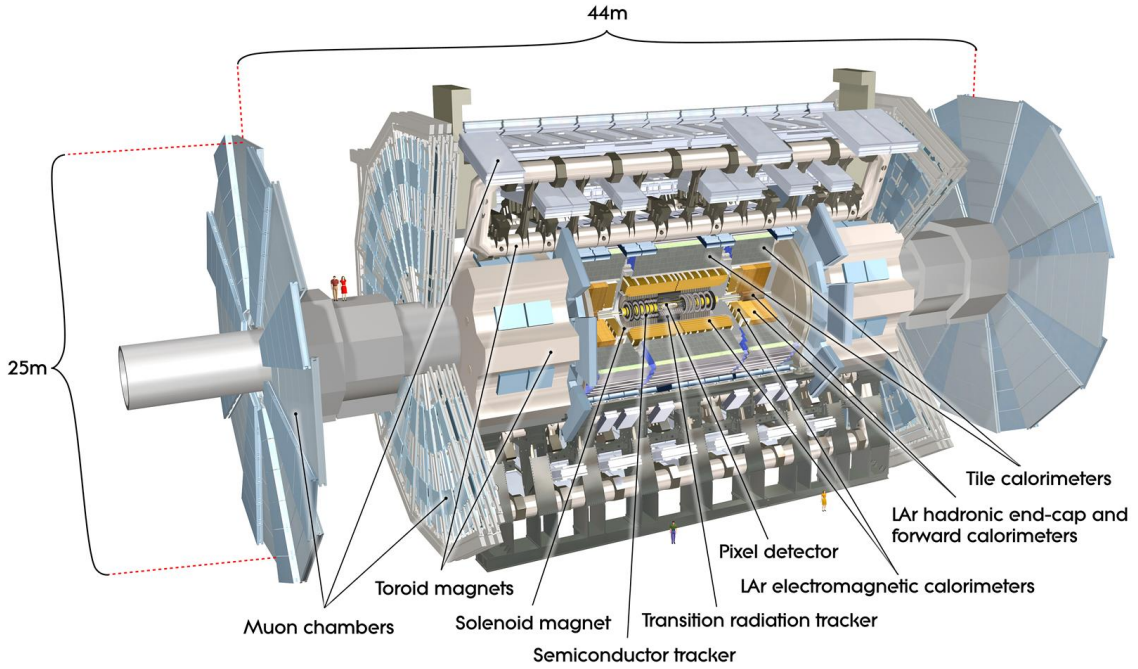


Figure 2.1: Overview of main parts of ATLAS - Inner Detector, Hadronic and Electromagnetic Calorimeters and Muon Detector, taken from [9].

and are replaced by cylindrical (or spherical) coordinates  $\phi, r, z$  ( $\phi, r, \theta$ ), where  $\phi = 0$  points in direction of  $x$  axis (and  $\theta=0$  points along the  $z$  axis). Another important parameter is *pseudorapidity*  $\eta$  defined as  $\eta = -\log \frac{\theta}{2}$  and *rapidity*  $y$  defined as  $y = \frac{1}{2} \log \frac{E+p_z c}{E-p_z c}$ . Advantage of rapidity is that it is additive under Lorentz transformation, whereas pseudorapidity is easier to determine, since it only depends on angle  $\theta$ . Both are equal for  $m = 0$  and they are popular in particle physics, since distribution of particles is almost constant when expressed in terms of  $y, \eta$ . In this analysis only pseudorapidity is considered. Sometimes, for simplifications, term forward (central) region will be used for high (low) values of  $|\eta|$ .

In the following section, basis of ATLAS trigger system will be explained. Then details of individual sub-detectors will be discussed. Emphasis will be put on the Inner Detector, since it is intrinsic part of tracking and therefore of the analysis.

### 2.2.1 ATLAS triggers

The ATLAS detector has various triggers. Part of the detector serves as Level 1 (L1) trigger, which reduces maximal 1 GHz rate of events to only 75 kHz. The event rate is further lowered by the high-level trigger to optimal frequency 200 Hz [10] (this is case for Run 1, situation in Run 2 will be different, probably 1kHz). Subset of L1, Minimum Bias Trigger Scintillators (MBTS), is used to select the events used in this analysis. It is made of polystyrene scintillator and is situated on the inner side of end-cap of electromagnetic calorimeters at  $z = \pm 3.56$  m and covers  $2.08 < |\eta| < 3.86$ . The MBTS is divided in inner and outer ring in  $|\eta| = 2.78$ , where outer ring has four segments and inner has eight. It is one of the parts of the detector, which was replaced between Run 1 and 2, and is optimized for low luminosity measurement, as for example Minimum Bias measurement [11].

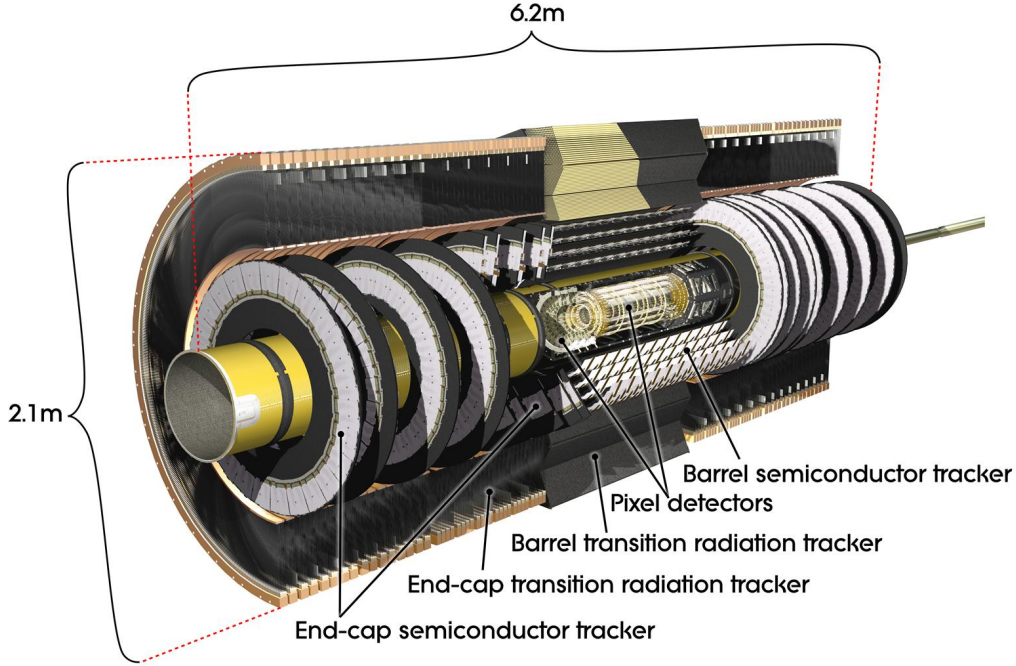


Figure 2.2: Overview of Inner Detector - barrel and end-cap, consisting of Pixel, SCT and TRT sub-detectors, copyright by **ATLAS Experiment © 2014 CERN** .

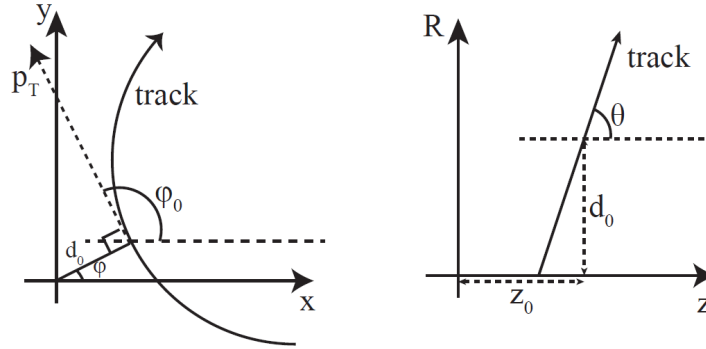
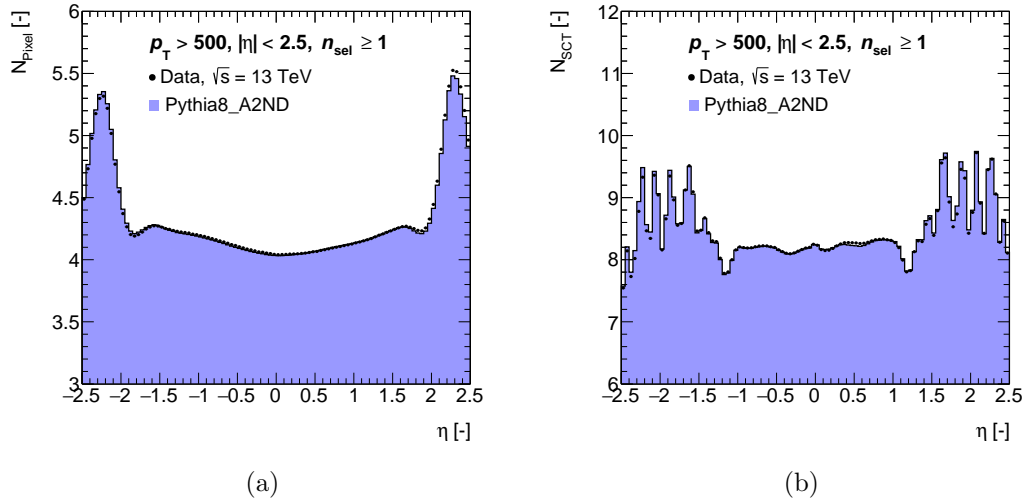
## 2.3 Inner detector

As can be seen in Figure 2.2, Inner Detector (ID) consists of three sub-detectors (Pixel, SCT and TRT) and two parts - barrel and end-caps. It is surrounded by a toroidal magnet with induction of 2T, which is shorter than the inner detector, resulting in a non-uniform field in the forward regions. Magnetic field causes deflection of charged particles in  $xy$  plane which is further used to determine  $p_T$ . The resolution of transverse momentum is  $\frac{\Delta p_T}{p_T} = 0.04\% p_T + 2\%$ , where  $p_T$  is in GeV.

Main purpose of the Inner Detector is reconstruction of tracks - trajectories of particles - and vertices - points of either collision of particle or of decays (which is later studied in section 3). In case of ATLAS, it is possible to reconstruct particle with  $p_T$  as low as 100 MeV. However, in most cases minimal  $p_T$  of the reconstruction is set to 400 MeV, with exception of e.g. minimum bias studies. In order to minimize energy losses and maximize efficiencies, material in detector is minimized as much as possible [12]. ID covers whole  $\phi$  region and  $|\eta| < 2.5$ .

Tracks are connected to another set of variables. Impact parameters define the distance of track's point of closest approach to the vertex. ATLAS uses two - longitudinal  $z_0$  coordinate, which is the distance alongside the  $z$  axis, and transverse impact parameter  $d_0$ , which is distance in the  $xy$  plane. Both definitions of impact parameters are illustrated in Figure 2.3. Transverse momentum  $p_T$ , part of momentum perpendicular to the  $z$  axis, is usually used instead of whole momentum, since it is invariant under Lorentz transformation and is directly determined from the curvature of particle trajectory. Another commonly used parameter is distance in  $\phi, \eta$  plane:  $R = \sqrt{\Delta\phi^2 + \Delta\eta^2}$ , which is used for example in fitting of tracks.

Position of interaction between particle and the detector is in case of the ID called hit. Absence of hit, when it is expected, is called a hole. There are various kinds of hits: ambiguous, when it is shared between two tracks, and module, when both layers of e.g. SCT detector are hit.

Figure 2.3: Definition of impact parameters  $d_0$  and  $z_0$ , taken from [13].Figure 2.4: Distribution of hits vs.  $\eta$  for (a) Pixel and (b) SCT detector, comparing data and Pythia 8 A2 simulation.

### 2.3.1 Pixel detector

Being closest to the beam and therefore to the collision, pixel detector must have large granularity to distinguish between large number of tracks and has to be able to resist great radiation. In  $R/\phi$  it has resolution of  $12 \mu\text{m}$  and in the  $z$  direction it has  $110 \mu\text{m}$  [12]. Area of the detector is approximately  $1.7 \text{ m}^2$  and it consists of three layers in both end-cap and barrel for Run 1. For Run 2, new layer - Insertable Beam Layer (IBL) - is added, which will be described individually.

Basis of the Pixel detector are 1744 identical sensors, where each is composed of 47233 pixels. Most pixels have proportions  $50 \times 400 \mu\text{m}^2$ , only 10% are  $50 \times 600 \mu\text{m}^2$ . Optimal temperature is  $-7^\circ\text{C}$  and voltage  $600 \text{ V}$ , but it is operational also at room temperature and with only  $150 \text{ V}$  [10].

Distribution of hits is in shown in Figure 2.4(a). Since it also contains the IBL, average number of hits approaches 4 in central region and 5 in forward regions.

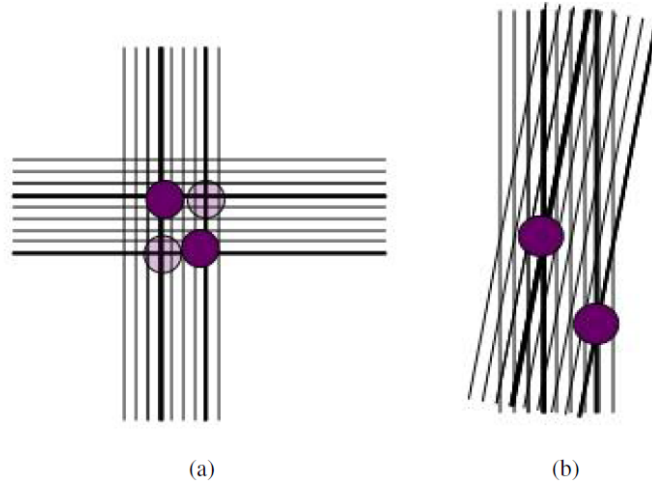


Figure 2.5: Two possible configurations of strip detector, a) perpendicular and b) under small angle, taken from [13].

### 2.3.2 Insertable Beam Layer

As was mentioned earlier, it is planned to increase frequency of collisions in the summer 2015. Because the former first layer (Blayer) will be more irradiated, it will be less efficient. To compensate for this, IBL was added, together with thinner beam pipe. This layer is only 3.3 cm from the center of the detector and has full  $\phi$  and  $|\eta| < 2.5$  coverage. Beam pipe going through the detector had to be reduced, from 2.9 cm to 2.5 cm, to make place for the IBL.

In order to cooperate with higher luminosities, size of the pixels was reduced from  $50 \times 400 \mu\text{m}^2$  to  $50 \times 250 \mu\text{m}^2$ . All the improvements should result in better tracking, impact parameter resolution and other improvements [14]. Better computation of impact parameter will also result in better vertex reconstruction and b-tagging.

### 2.3.3 SCT detector

SCT (Semi Conductor Tracker) has barrel and end-cap, where barrel covers  $|\eta| < 1.4$  and consists of four layers, end-caps cover  $1.4 < |\eta| < 2.5$  and consist of 9 layers on each side. There are 15912 silicon sensors, which operate on minimal voltage 150 V and optimal voltage 250-350 V [10]. Resolution is  $9 \mu\text{m}$  [12]. Each layer consists of two back-to-back layers, which are necessary, since SCT is strip detector. In order to properly define hit, there needs to be hit in each layer and strips in those layers must not be parallel. There are two ways to approach this. They may be perpendicular, which ensures the most precise coordinates. However it may result in ghost hits, as can be seen on picture 2.5(a). Other possibility, used in ATLAS, is to have a small angle between strips (in case of ATLAS it is  $\approx 10^\circ$ ), which leads to smaller precision, but lowers chance of false hits [13]. Hit distribution for SCT can be seen in Figure 2.4(b). Average number of hits is around 8 with more complicated structure in forward region.

### 2.3.4 TRT detector

Transition Radiation Tracker (TRT) is the outer-most detector of the inner detector. Again, it consists of barrel ( $|\eta| < 2$ ) and end-cap ( $1 < |\eta| < 2.5$ ). Basic unit is a straw, which is parallel to the beam

pipe for barrel and perpendicular for end-caps. This leads (for barrel) to good resolution in  $xy$  and consequently to poor resolution of  $z$  coordinate.

Straws of the TRT detector have a diameter of 4 mm and are composed of thin wire in gas (70% Xe, 27% CO<sub>2</sub>, 3% O<sub>2</sub>). The gas gets excited and ionized by passing particle. Due to electrical field, electrons and ions create a current, which can be measured. With this information, distance of the trajectory from the wire can be determined from the drift time.

TRT detector has also another function - it can distinguish between electrons and other particles. The space between straws is filled with a radiative material. When a particle passes the border of this material, X-rays are emitted (due to transition radiation, hence the name). Since this radiation is proportional to  $E/m$ , it is by far strongest for electrons. The emitted photons cause another excitation in the straws. For this reason, TRT has two thresholds, one for the measurement of passage of particle and one for the electron identification.

## 2.4 Calorimeters and muon spectrometer

Calorimeters are used mainly to find out energy of particles by stopping them and measuring deposited energy. They usually have absorber part, which stops the particle, and sampling material. They are not significant for this analysis and are mentioned only briefly.

**Electro-magnetic calorimeter** - main goal is to measure electrons and photons. It has lead absorber and liquid argon for sampling. It covers whole  $\phi$  region and is composed of barrel and two end-caps with total coverage  $|\eta| < 3.2$ . The resolution in energy is  $\Delta E/E = 11.5\%/\sqrt{E} + 0.5\%$  and for  $\phi$ ,  $\Delta\phi = 50/\sqrt{E}$  mrad, where in both cases energy is in GeV [12].

**Hadronic calorimeter** is placed around EM calorimeter and consists of 3 parts. Its barrel covers  $|\eta| < 1.7$  and is made up of steel absorber and scintillators. Hadronic end-cap calorimeter uses different materials, copper as absorber and liquid argon as sampling material, and covers  $|\eta| < 3.2$ . Forward calorimeter covers  $|\eta| < 4.9$  and is made of combination copper+liquid argon and tungsten+liquid argon [13].

**Muon spectrometer**, as the name suggests, measures only muons, strictly speaking high  $p_T$  muons. It consists of 3 barrel layers in 5, 7.5 and 10 meters from the beam pipe and  $2 \times 3$  end-caps at  $\pm 7.9, \pm 14, \pm 21.5$  meters. It consists of many sub-detectors: muon drift tubes, cathode strip chambers, resistive plate chambers and thin gap chambers. Their description is however beyond the scope and interest of this thesis.

# Chapter 3

## Tracking

Reconstruction of tracks is important part of the analysis. At first, general algorithms used on ATLAS will be introduced, before moving to information specific to the measurement. Some description of vertexing will also be presented, since it is intrinsic part of the tracking process.

### 3.1 Tracking algorithms

Tracking means reconstruction of trajectories of particles only based on the detector information. Basic units used for tracking are space points, which are derived from detector hits. This can be done easily in case of the Pixel detector, however strip detectors, as e.g. the SCT, do not have precise space-point information. In such case, hits in both layers are needed, combined with beam line information, where beam line refers to average position of vertices.

In general, the tracking is composed of three steps. First is a pattern recognition, stage during which track candidates are created from hits. Then ambiguity solving, since reconstructed tracks can share hits. And finally, tracks are (re-)fitted to get the most precise results.

Quality of tracks is influenced by multiple factors, e.g. by number of hits a particle creates or resolution of the detector. Another factor is an energy loss of particles due to interaction with detector. To reduce this effect, detector material must be estimated as precisely as possible and taken into account in the reconstruction. This cannot be done only from technical drawings, other - data driven - techniques are needed. For example, studying decay of  $K_S^0$  to two charged pions or a rate of secondary vertices due to hadronic interaction versus  $R$ , the radial distance from the beam line, can lower the uncertainty on detector material under 10% [13].

There are two basic algorithms used in tracking - inside-out and outside-in. The latter is not that important for us, since its contribution is small.

#### 3.1.1 Inside-out algorithm

This algorithm is the main part of New Tracking (NewT) in ATLAS [15]. As the name suggests, inside-out algorithms starts from the inner parts of the detector. Three space-points are used to create so called seed of track. Based on trivial formula for Lorenz force, transverse momentum  $p_T$  is computed:  $p_T = qB\rho$ , where  $q$  stands for charge of the particle,  $B$  for magnetic induction and  $\rho$  is radius of the trajectory [16]. If  $p_T$  satisfies minimal value (dependent on type of algorithm), the seed is used as basis of a track candidate. This way, all hits are utilized to create seeds. Values of longitudinal impact parameter of the seeds are filled in histogram based on  $p_T$ . With this information, candidate for primary vertex (PV) is determined. If more vertices are present primary vertex corresponds to vertex with highest sum of  $p_T$  of tracks.

In the next step, algorithm extrapolates individual seeds and searches for additional hits. Large number of track candidates is created, with only one track candidate per seed [13]. It is obvious,

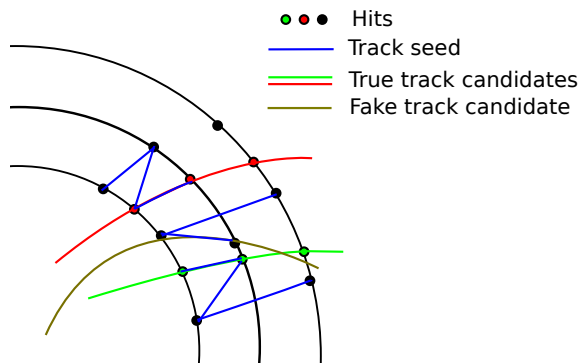


Figure 3.1: Illustration shows roughly process of inside-out tracking. First, track seeds are created from small number of hits and those are then extended to other layers of detector. This way, track candidates of real particles arise alongside with fake tracks. Not all track seeds result in track candidate

that not only tracks of real particles are reconstructed. Many tracks which are made from random hits, are also produced. They do not belong to any particle and are called fake track. To lower their contribution, score system is implemented. Every track receives score based on numerous parameters. For example, a penalty is given, when there is a hole in Pixel layer. Hits belonging to several tracks are then assigned to the track with highest score and remaining tracks are refitted without those hits. This procedure is repeated several times, until all ambiguous hits are resolved. Only tracks with score higher than certain predetermined value are further used. Simple diagram showing track seeds and track candidates is in Figure 3.1.

Track candidates can now be expanded to the TRT sub-detector, based on compatibility of hits and the track candidate. No new tracks are created in this stage.

### 3.1.2 Outside-in algorithm

Disadvantage of inside-out tracking is large density of hits near the beam pipe. As a result, fake tracks are created and some real tracks may be discarded by the elimination process. Furthermore, secondary particles created beyond Pixel layer may not have enough hits in silicon sub-detectors and thus not be recreated.

Outside-in algorithm starts with seeds created in TRT, which are then backtracked to silicon detectors. The advantage of this algorithm originates from lower particle density. On the other hand, some short-lived particles may not be able to reach the TRT detector and are not reconstructed. It is therefore appropriate to use inside-out algorithm first and then the outside-in to reconstruct remaining particles. Since in our case we have requirements on hits in pixel and SCT layer, only negligible number of tracks is reconstructed by the latter method.

## 3.2 Vertex reconstruction

As was mentioned earlier, based on impact parameter  $z$  and transverse momentum  $p_T$ , candidate for vertex is created. Tracks not associated with this vertex are then discarded and vertex is refitted. This can be repeated several times. Discarded tracks are used to find another vertex seed. Primary vertex is then determined from the requirement on the highest sum of transverse momentum.

Another possibility is to fit several vertices at same time. Every iteration, new vertex is seeded and then fitted together with all previous. Tracks are then associated with a particular vertex based on certain compatibility criterion. Finding of vertices is easier, if beam line position is known in advance.

## Chapter 4

# Strategy behind current measurement

In first part of this chapter, selection of events and tracks for this analysis will be discussed. After that, background of the measurement is described. Final part of this chapter will focus on basic principles behind corrections.

### 4.1 Clasification of tracks and vertices

As was mentioned in the introduction, particles studied in this thesis are charged primary particles. With those we associate primary tracks, which can be properly identified only in Monte Carlo where we are to certain level able to match tracks and particles. Matching of tracks and particles will be more explained in latter section of Chapter 5. Non-primary tracks can be either secondary tracks from secondary particles or fake tracks, which are results of random combination of hits.

Vertices can be also subdivided in subgroups. Primary vertex was already defined as vertex with highest sum of  $p_T$ . All other vertices from same bunch crossing are called pile-up and vertices due to particle decays are then referred to as secondary vertices.

### 4.2 Selections

As in every measurement, certain selection must be implemented to assure some quality of studied objects. In our case two main selections are used - event and track selection. The former selects events mainly based on vertices and triggers, the latter examines properties of tracks as e.g. transverse momentum or number of hits.

#### 4.2.1 Event selection

Even though it may not be obvious, event selection has influence on quality of tracks. It can minimize contribution of non-primary tracks due to beam background.

Minimum bias measurement are made with as little selection as possible. It is required that single-arm<sup>1</sup> MBTS trigger must be fired. The MBTS is sensitive to wide spectrum of particles and is therefore ideal for inclusive measurement. Trigger hit is only required for data, for Monte Carlo is the selection omitted since the trigger information is not present.

---

<sup>1</sup>Meaning at least one of the end-caps must have hit above some threshold

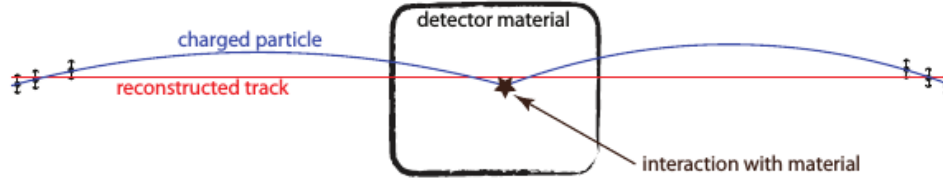


Figure 4.1: Picture of possible process leading to higher reconstructed momentum, taken from [17].

Furhermore, primary vertex is a required and events with second vertex with four or more Other regions are studied, but the main region has larger priority and must be finished firsttracks are rejected. This removes events with more that one interaction of colliding bunches.

There is additional selection based on number of tracks in certain phase-space region. The region studied in this thesis requires at least one track with  $p_T > 500$  MeV,  $|\eta| < 2.5$ . There are other regions used in course of the measurement in order to study some dependencies, for example phase-space with two tracks with  $p_T > 100$  MeV is used to determine tracking efficiency.

## 4.2.2 Track selection

In order to minimize low quality tracks, additional selection is needed. Reconstructed tracks are required to have at least 100 MeV. Next, selection is on number of hits of tracks. Problem is that sometimes particle passes through nonfunctional sensor, so called dead sensor, and is not registered by it. In such case it may not pass the selection, even though it has required properties. Therefore if hit is expected in place with dead sensor, it is sometimes counted as if the sensor was hit by the particle.

First hit selection is connected to the new IBL. In previous analysis, hit in BLayer, first layer in the analysis, was required if it was expected. Current selection requires IBL hit if it is expected, and if not, BLayer hit is required if it is to be expected. This also reduces number of secondary tracks, because they often originate further from beam line and do not come through the IBL or BLayer. Aside from this selection, at least one hit or dead sensor in whole Pixel detector is required (including IBL and BLayer).

In order to lower contribution of secondary tracks, additional cut on impact parameters is applied:  $|d_0^{BL}| < 1.5$  mm and  $|z_0^{PV} \cdot \sin \theta| < 1.5$  mm, where PV means impact parameter is used in regards to primary vertex, which is required by the event selection, and BL means in regards to position of the beam line. However, sometimes events with not primary vertex are considered, in that case no cut on  $z_0$  is applied. Distribution of secondary tracks will be discussed later, but for demonstration, Figure 4.2 shows their distribution for small kinematic region, demonstrating primary tracks dominate for low values of  $d_0$ .

One of the problems connected with reconstruction of particle is migration. Particles are not always reconstructed with right kinematics such as  $p_T$ . This effect is solved by so-called unfolding, which will be discussed in later section. Sometimes, however, particle with small momentum interacts with material or decays and tracking algorithm may reconstruct it with much higher momentum. Example of this can be seen in Figure 4.1. As will be visible in figure with final results,  $p_T$  spectrum falls quickly and only small fraction of tracks migrating to bins with high momentum changes spectrum drastically (for more see [17, Figure 2]).

In order to minimize this effect, additional selection is applied. First, number of SCT hits is  $p_T$  dependent. For tracks with  $p_T > 100/300/400$  MeV number of SCT hits plus dead sensors must be  $\geq 2/4/6$ . There was a similar cut in previous analysis, only with  $p_T > 100/200/300$  MeV, where without this selection number of badly reconstructed tracks in  $30 < p_T < 50$  GeV was around 90%, but with this selection it was only 32% [18]. In our case the  $p_T$  values were changed in order to

increase tracking efficiency. As can be seen in Figure 2.4, average number of pixel hits is greater than 3 and number of SCT hits is greater than 7, meaning majority of tracks is indeed unaffected by those selections.

Another way to reduce mis-measured tracks is to cut on  $\chi^2$  probability.  $\chi^2$  represents value determining quality of fit for tracks. It is value retrieved from method of the least squares - distance between hits and reconstructed track summed in quadrature. Probability is then computed as  $1 - P(n_{dof}/2, \chi^2/2)$ , where  $n_{dof}$  is number of degrees of freedom and P is incomplete gamma function. It stands for probability that observed  $\chi^2$  is greater than value of correct model.

## 4.3 Background

As for any measurement, one of factors which must be taken in consideration is background. Background effects for events are:

**Cosmic rays** have contribution smaller than  $10^{-6}$ . Lowering the contribution of cosmic rays is the main reason why was LHC build deep under ground.

**Beam-induced background.** Even though there is almost complete vacuum in the tubes, there is still some small fraction of particles left. Sometimes particle from the beam can collide with particle from the left-over gas. Those however create only 0.1% of all selected events, thanks to requirement on primary vertex.

**Pile-up**, or presence of another collision in the same bunch crossing. Contribution of pile-up is however higher than that of previously mentioned cases and therefore cannot be neglected. This is reason why events with second vertex (with 4 or more tracks) are rejected in event selection, lowering the contribution to circa 0.1%.

### 4.3.1 Background to primary particles

Not all particles coming from collision are primary and detector cannot directly distinguish between primary and non-primary particles. For this reason, contribution of primary and secondary tracks must be estimated. As was mentioned in previous chapter, reduction of secondary tracks is main reason for implementation of cut on impact parameters.

Secondary particles/tracks can have various origin - hadronic interactions, photon conversions, decays of long-lived particles etc. Secondaries are further divided between electrons and non-electrons, since electrons mostly come from material conversions and are therefore sensitive to detector modeling. Distribution of all those components can be found in Figure 4.2. They are derived from Monte Carlo generators and their relative fraction is then determined from data by a fit. This fit is done for region  $|d_0| > 5$  mm.

Since primary particles originate in vertex, they have usually low  $d_0$ . In studied region, their contribution is almost 100 times bigger than that of secondaries. Together with requirement on BLayer is the contribution of secondaries fairly low. Those left are accounted for in corrections.

## 4.4 Weight corrections

After the selection, distributions need to be corrected for effects of the detector. Those corrections can be more straight-forward, like applying weights to tracks, or more complicated, such as Bayesian unfolding. Here, correction by weight is described, using various efficiencies.

Since event weight compares events with and without primary vertex, the parametrization cannot use selection described at beginning of this chapter, since that one requires PV. Instead, looser selection

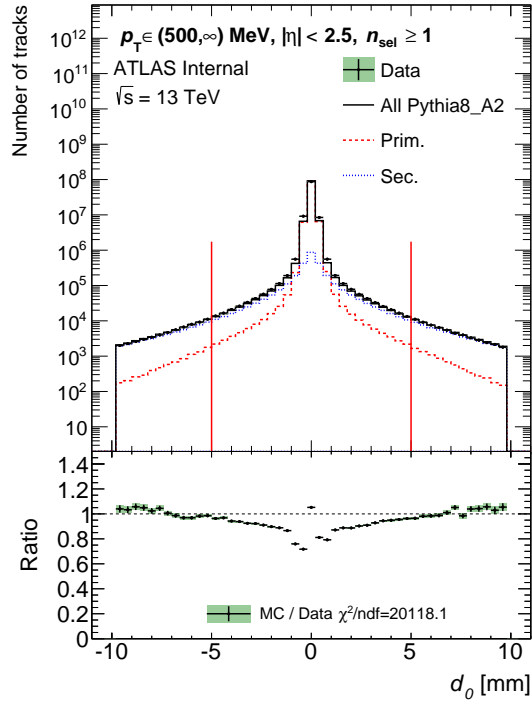


Figure 4.2: Distribution of primary particles, electrons and secondaries without electrons for  $\sqrt{s} = 13$  TeV. Monte Carlo, in this case Pythia 8 A2, is fitted on data to estimate contribution of secondary particles. Courtesy to Jiří Kvita, not final version of the plot.

with no cut on  $z_0$  is defined and event weight is described using variable  $n_{sel}^{BL}$  - number of tracks, which pass this selection in given event.

Consider now, that the detector reconstructs vertex with an efficiency  $\varepsilon_{vtx}(n_{sel}^{BL}, x)$ , where  $x$  can be some other variable, examples of which will be shown in next chapter. Also consider trigger efficiency  $\varepsilon_{trg}(n_{sel}^{BL})$ . Then event weight is defined in this way:

$$w_{ev}(n_{sel}^{BL}) = \frac{1}{\varepsilon_{trg}(n_{sel}^{BL})} \cdot \frac{1}{\varepsilon_{vtx}(n_{sel}^{BL}, x)} \quad (4.1)$$

Track weight is more complicated than event weight. In addition to the inefficiency of detector one must also correct for non-primary particles. Furthermore, particle outside our kinematic region can be due resolution of detector reconstructed within the studied phase-space. Reverse effect, particle within the kinematic region migrating outside, is already taken into account by tracking efficiency. Finally, strange baryons must be excluded, since they are not longer considered as primary particles.

Fraction of the non-primary tracks is designated as  $f_{nonp}(p_T)$ , fraction of the migrating tracks as  $f_{okr}(p_T, \eta)$  and fraction of strange baryons as  $f_{SB}(p_T)$ . If we take track reconstruction efficiency as  $\varepsilon_{trk}(p_T, \eta)$ , then the track weight is:

$$w_{trk}(p_T, \eta) = \frac{1}{\varepsilon_{trk}(p_T, \eta)} \cdot (1 - f_{okr}(p_T, \eta) - f_{nonp}(p_T) - f_{SB}(p_T)) \quad (4.2)$$

Technical implementation includes strange baryons as secondary particles.

Both weights are used to account for particles and events we were not able see or which were reconstructed with wrong properties. Efficiencies are properly described in following chapter.

# Chapter 5

## Tracking and vertexing efficiencies

This chapter covers derivation of tracking and vertexing efficiencies. Method used to match tracks and particles is also described. Further, fraction of secondary tracks and migration of primaries are discussed.

Trigger efficiency is omitted since it was not done by me. It is used only on data and affects mainly events with small number of selected tracks and it has smaller effect than vertexing efficiency.

### 5.1 Vertex reconstruction efficiency

Vertices are reconstructed using tracks and information about beam line. Vertex efficiency is therefore in general dependent on the tracking efficiency. To separate vertex and track efficiency as much as possible, the vertex efficiency is determined as function of number of reconstructed and selected tracks.

Dependence of the efficiency on other observables is also studied. Strong dependence is found in events with  $n_{sel}^{BL} = 2$  on longitudinal distance  $\Delta z$  between the tracks or on  $\eta$  if only single track is present.

Vertexing efficiency is determined from reconstructed spectra, which in this case means either from data when used on data or from track level of Monte Carlo when used on Monte Carlo.

#### 5.1.1 Vertex efficiency vs. $n_{sel}^{BL}$

Vertex efficiency for each bin is taken from data as a fraction of events with and without reconstructed vertex. This is done for all kinematic regions, in our case for phase-space regions (a)  $n_{ch} \geq 2, p_T > 100$  MeV and (b)  $n_{ch} \geq 1, p_T > 500$  MeV. Results are visible in Figure 5.1.

Efficiency is 1 for  $n_{sel}^{BL} > 4$  for both phase-spaces and for both data and Pythia 8. This is to be expected, since bigger number of tracks means more information is used to reconstruct the vertex. Lowest efficiency is in  $n_{sel}^{BL} = 2$  of the first kinematic region, where it is around 88% for Monte Carlo and 86% for data. Efficiency in first bin of the second phase-space is 93% for Monte Carlo and slightly under 90% for data.

It may seem to be odd, that for  $n_{sel}^{BL} = 1$  in case of second phase-space, the vertex efficiency is higher than for  $n_{sel}^{BL} = 2$  for the first one. This is because for every track with  $p_T > 500$  MeV, there are on average more than 3 tracks for data or 5 tracks for MC with  $p_T > 100$  MeV, as can be seen in Figure 5.2), which shows correlation between number of selected tracks between both kinematic regions.

#### 5.1.2 Vertex efficiency vs. $\Delta z_0$ for $n_{sel}^{BL} = 2$

Strong dependence on the longitudinal distance between tracks is observed and therefore its implementation into correction procedure leads to better results It is defined only for phase-space with at least two tracks with  $p_T > 100$  MeV, since in the second region the dependence is negligible. Definition of

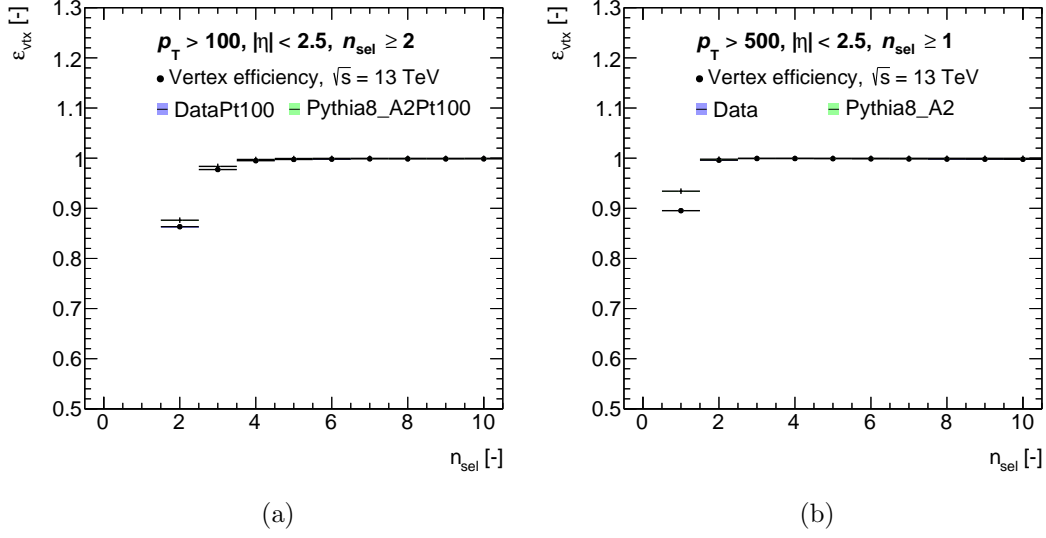


Figure 5.1: Vertex efficiency vs.  $n_{\text{sel}}^{BL}$  for phase space regions (a)  $n_{ch} \geq 2, p_T > 100$  MeV and (b)  $n_{ch} \geq 1, p_T > 500$  MeV, displayed for both data and Pythia 8 A2 simulation.

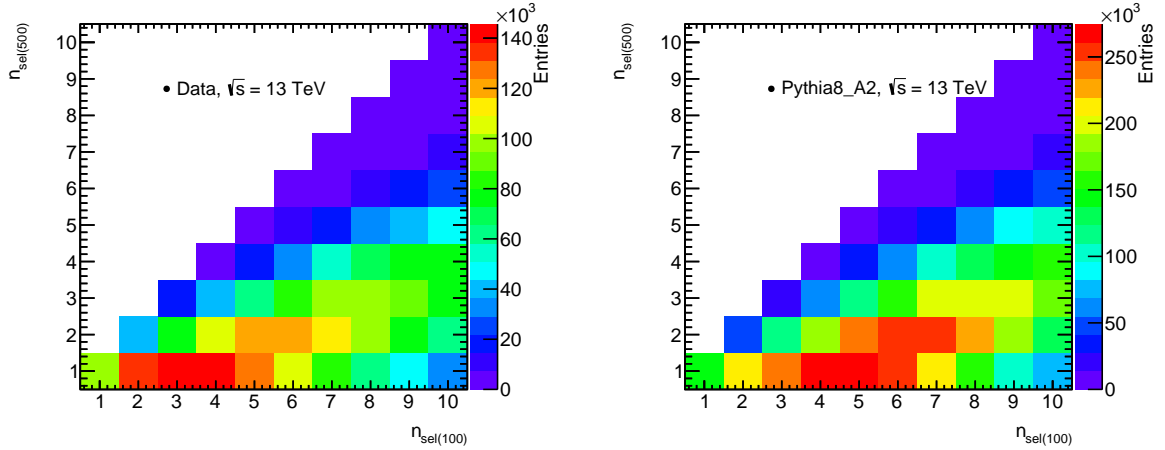


Figure 5.2: Correlation between  $n_{\text{sel}}^{BL}$  for phase space regions  $n_{ch} \geq 2, p_T > 100$  MeV, denoted as  $n_{\text{sel}}(100)$ , and  $n_{ch} \geq 1, p_T > 500$  MeV, denoted as  $n_{\text{sel}}(500)$ . No vertex requirement is applied.

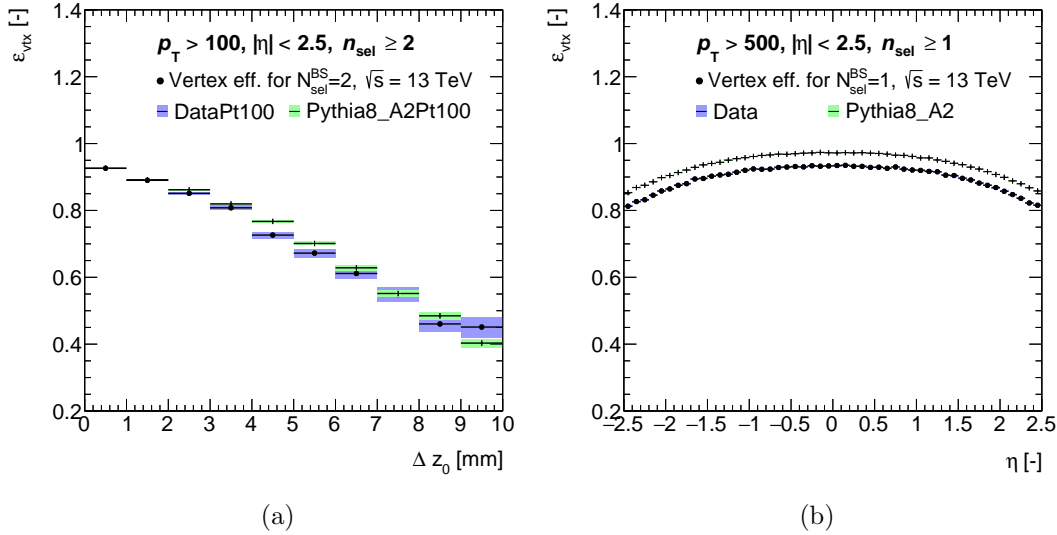


Figure 5.3: Vertex efficiencies for lowest  $n_{\text{sel}}^{\text{BL}}$  bins in given phase-space, (a) Vertex efficiency for  $n_{\text{sel}}^{\text{BL}} = 2$  vs.  $\Delta z$  for phase-space regions  $n_{\text{ch}} \geq 2, p_T > 100$  MeV, (b) Vertex efficiency for  $n_{\text{sel}}^{\text{BL}} = 1$  vs.  $\eta$  for phase space region  $n_{\text{ch}} \geq 1, p_T > 500$  MeV. Displayed for both data and Pythia 8 A2.

efficiency is same as in previous case, only the dependence on  $\Delta z$  instead of on  $n_{\text{sel}}^{\text{BL}}$  is studied. Results are in Figure 5.3a.

As expected, closer the tracks are<sup>1</sup>, the greater is the chance to reconstruct vertex. The efficiency for MC starts at around 90% for  $|\Delta z_0| < 1$  mm and falls almost linearly to circa 30% at  $9 < |\Delta z_0| < 10$  mm. For data is the distribution similar, though on average it is smaller, which is in agreement with what is in first bin in Figure 5.1a.

### 5.1.3 Vertex efficiency vs. $\eta$ for $n_{\text{sel}}^{\text{BL}} = 1$

Another significant dependence of vertex efficiency is on the pseudorapidity of track, when only one track is present ( $n_{\text{sel}}^{\text{BL}} = 1$ ). Since only one track is required, only the region with  $p_T > 500$  can be considered. Average efficiency for only one particle is 90% in data. As can be seen of Figure 5.3b, the efficiency for MC is smallest in forward regions (down to 80% at  $|\eta| = 2.5$ ) and biggest at central region with around 95% at  $\eta = 0$ . For data the shape is almost the same, but the efficiency is lower in all bins, which is in agreement with what we see in first bin in Figure 5.1b.

## 5.2 Tracking efficiency

Tracking efficiency is determined from the Monte Carlo and is defined as a ratio of primary particles matched to reconstructed tracks within kinematic region  $p_T > 100$  MeV and  $|\eta| < 2.5$  and all primary particles:

$$\varepsilon_{\text{trk}}(p_T, \eta) = \frac{N_{\text{gen}}^{\text{matched}}}{N_{\text{gen}}}(p_T, \eta), \quad (5.1)$$

where primary particle must be within the studied kinematic region. Both components are studied with regards to  $p_T, \eta$  of generated particle, not of the reconstructed tracks. Dependence on  $n_{\text{ch}}$  was studied and is negligible. Again, both kinematic regions were investigated and it has been determined

<sup>1</sup>More precisely distance between the points of closest approach to beam line

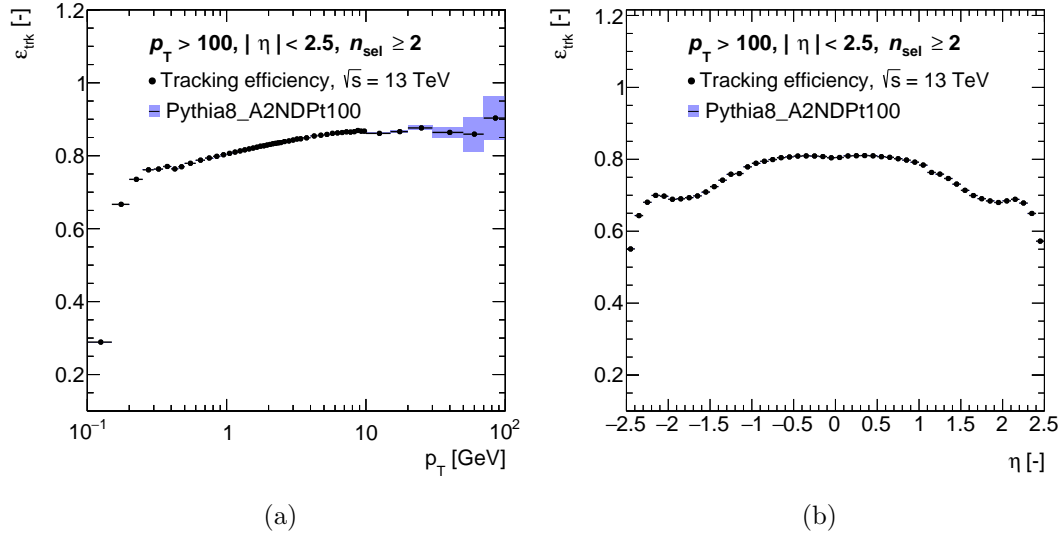


Figure 5.4: Tracking efficiency vs. (a)  $p_T$  and (b)  $\eta$ , determined from non-diffractive Pythia 8 A2 sample with  $\sqrt{s} = 13$  TeV.

that efficiencies are not different for both phase-spaces for  $p_T > 525$  MeV. For this reason only the one for  $n_{ch} \geq 2, p_T > 100$  MeV can be used.

### 5.2.1 Matching reconstructed and truth particle

For many reasons a track can't be definitely linked to a particle. Either it is a fake track, or it was so poorly reconstructed, that it does not have almost anything common with the original particle. Therefore a truth matching probability must be defined and then cut implemented to get matching between reconstructed track and truth particle.

In our case, truth matching probability is defined using hits in Pixel, SCT and TRT detector:

$$P_{truth} = \frac{10 \cdot N_{Pix}^{truth+reco} + 5 \cdot N_{SCT}^{truth+reco} + 1 \cdot N_{TRT}^{truth+reco}}{10 \cdot N_{Pix}^{reco} + 5 \cdot N_{SCT}^{reco} + 1 \cdot N_{TRT}^{reco}}, \quad (5.2)$$

where  $N_X^{truth+reco}$  is number of hits in sub-detector X from both truth and reconstructed tracks and  $N_X^{reco}$  is number of hits from the reconstructed track. In case of this analysis, track is considered as matched to primary particle when it has  $P_{truth} > 50\%$ . This value is determined from studies of distributions of primary and secondary tracks. For more information see [6].

### 5.2.2 Tracking efficiency vs $p_T$ and $\eta$

Results of tracking efficiency are in Figures 5.4 and 5.5. Track efficiency vs  $p_T$  starts fairly low at 10-15% for  $p_T \approx 100$  MeV and is raising sharply to 70-75% at 300 MeV and  $>80\%$  for  $p_T > 10$  GeV. Efficiency increases because particle with higher  $p_T$  gets further through the detector, therefore acquires more hits and has greater chance to get reconstructed properly.

Dependence on  $\eta$  is not so sharp, starting on 50-55% in most forward region and raising to 80% in central region. Efficiency is small in forward regions because particle must pass through larger amount of material. Thus particle loses energy or is scattered, making it harder to reconstruct it properly.

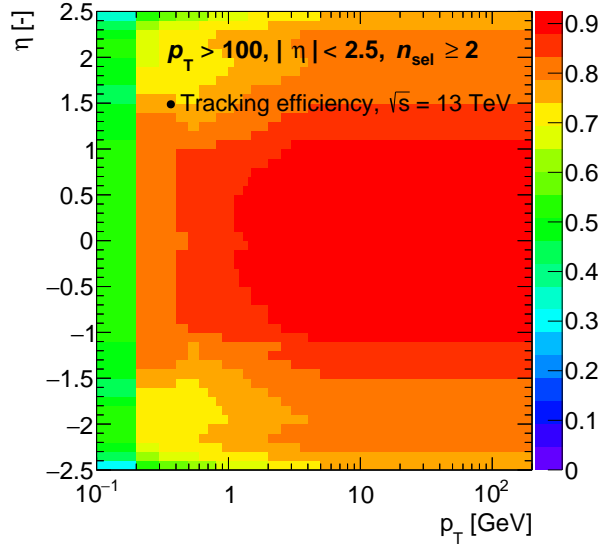


Figure 5.5: Tracking efficiency for phase space region  $n_{ch} \geq 2, p_T > 100$  MeV in  $p_t$  vs.  $\eta$ . Determined from non-diffractive Pythia8 A2 sample.

### 5.3 Secondary particles

As was mentioned before, fraction of secondary particles is reduced by implementing the  $d_0$  and  $z_0$  cut, but further corrections are needed. Fraction of secondary particles is determined as ratio of tracks matched to secondary particle and of all selected tracks. The fraction is studied in regards to  $p_T, \eta$ , however the dependence on  $\eta$  is minimal for  $p_T > 500$  MeV. The fraction of secondary particles is about 3 % for  $p_T = 100$  MeV and decreases to about 1% for 10 GeV, as can be in Figure 5.6.

For region  $100 < p_T < 500$  MeV dependence is studied for electrons and non-electrons separately. Their distribution and fraction of secondary particle in general are in Figure 5.7. It is obvious that both components have completely different spectra and dependence on  $\eta$  is more significant. Electrons are more prominent at low  $p_T$  and forward region, non-electrons have more balanced spectrum with two significant bumps in  $|\eta| \approx 2, p_T = 200 - 400$  MeV.

### 5.4 Tracks migrating to kinematic region

Since the detector has finite resolution, particles which are outside the required phase-space may be reconstructed as if they were inside, or may migrate between bins. Tracking efficiency and unfolding, which will be described in following chapter, effectively correct for migration between bins. Bigger problem are tracks near the edge of the defined phase-space. Since efficiency is derived for  $p_T > 100$  MeV, even though studied phase-space is for  $p_T > 500$  MeV, migration to  $p_T < 500$  MeV is not considered, since it is effectively compensated by migration from that region. The migration factor therefore corrects only for tracks matched to primary with  $|\eta| > 2.5$ .

Obviously, fraction of those tracks is defined as ratio of selected tracks with matched particle outside of the kinematic region and of all matched (primary and secondary) tracks. As can be seen in Figure 5.8, this migration is really small, significant only at the border bins and for low  $p_T$  (in whole  $\eta$  region). This migration is always lower than 10% and aside from boundary bins is lower than 1%.

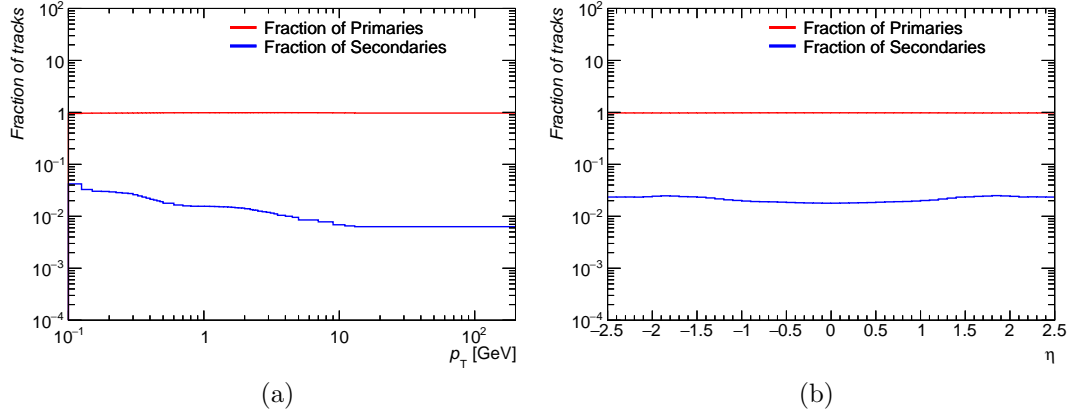


Figure 5.6: Fraction of secondary particles vs. (a)  $p_T$  and (b)  $\eta$ , determined from non-diffractive Pythia 8 sample with  $\sqrt{s} = 13$  TeV.

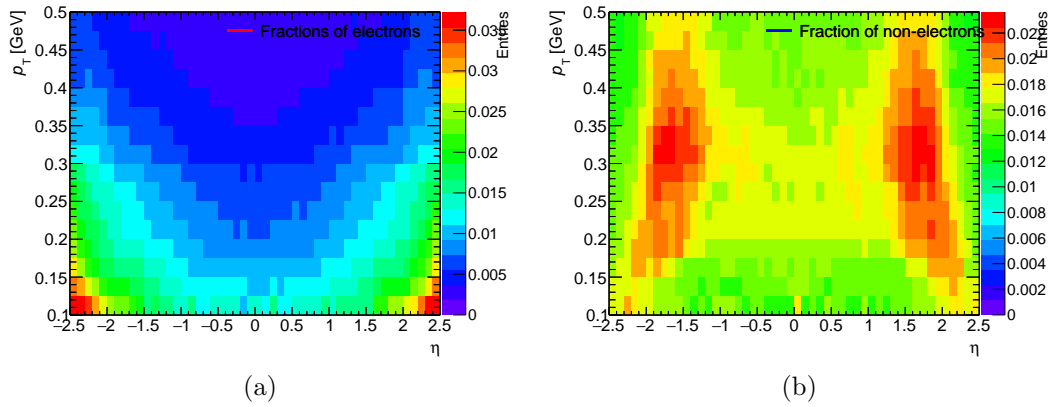


Figure 5.7: Fraction of (a) electrons, (b) non-electrons, determined from non-diffractive Pythia 8 A2 sample with  $\sqrt{s} = 13$  TeV.

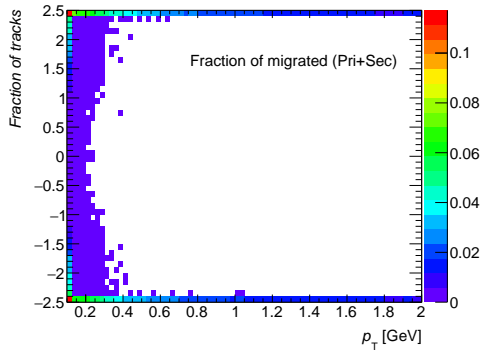


Figure 5.8: Fraction of tracks which migrated outside of the kinematic region  $n_{ch} \geq 2, p_T > 100$  MeV as function of  $p_T, \eta$ . Determined from Pythia 8 A2 sample.

# Chapter 6

## Corrections

This chapter goes through correction process and compares various stages of corrections. First, unfolding is described as it is the most important correction procedure aside from weights, since it corrects for migration of tracks due to resolution of the detector. The  $p_T, n_{ch}, < p_T >$  must be corrected by the unfolding, only the  $\eta$  distribution does not suffer by a significant migration.

I worked on the  $p_T, \eta$  and  $< p_T >$  distributions, but the  $n_{ch}$  spectrum is also discussed, since it is further used in the other distributions and description of the correction procedure would be incomplete without it.

### 6.1 Unfolding

Full description of unfolding is beyond the scope of this thesis. Only basic idea of unfolding will be explained, with examples and applications demonstrated in later sections. All information about unfolding is based on reference [19]

In any analysis there are two main spectra we must consider. One we will call truth  $t$ , which describes real distribution in nature, and reconstructed  $r$  (reco), which is obtained with the detector. Our output is usually discrete and can be obtained from truth by *response matrix*  $R$  through simple formula  $r = Rt$ . This process is called *folding*. However, what we usually want is the opposite procedure - getting real situation based on the measured spectra - called unfolding.

First solution, which comes to mind, is to invert matrix  $R$ , thus getting wanted relation  $t = R^{-1}r$ . This however works only in theory, since expected observed distribution is different from the reconstructed spectrum. For example statistical fluctuation can be "interpreted" as presence of some structure, which was affected by the detector resolution. This leads to oscillating solutions and for this reason other methods are used, as for example Bayesian unfolding, which was applied in our case.

#### 6.1.1 Bayesian unfolding

As the name suggests, Bayesian unfolding is based on Bayes' theorem. Considering we have probability densities for true and reconstructed spectrum  $f(true), g(reco)$ , the theorem can be written as

$$P(true|reco) = \frac{P(reco|true)f(true)}{g(reco)}, \quad (6.1)$$

where  $P(true|reco)$  is probability of true given reco (and vice versa for  $P(reco|true)$ ).  $f(true)$  can be derived thus:

$$f(true) = \int g(reco)P(true|reco)dreco, \quad (6.2)$$

but this obviously assumes knowledge of  $P(true|reco)$ . Bayesian unfolding uses Bayes' theorem and by iterative process determines the best possible approximation of this function. First iteration is derived from MC - we get  $P(reco|true)$ ,  $f(true)$  - and then we plug it together with observed  $g_{data}(reco)$  to the Bayes theorem to get  $P(true|reco)$ , which we substitute to the equation and get first iteration  $f^0$ . Next iteration is then defined as

$$f^{r+1}(true) = \int f^r(true) \frac{g_{data}(reco)}{g^r(reco)} P(reco|true) dreco \quad (6.3)$$

where  $g^r(reco) = \int f^r(true) P(reco|true) dtrue$ , which is equation similar to Eq. 6.2. Specific method used in our case is called D'agostini's scheme.

Practical implementation is done more or less in this way: First we apply weights derived from efficiencies on raw spectra. Using MC we gain migration (or more precisely corresponding) matrix, which is matrix of  $X^{true}$  vs.  $X^{reco}$ , where  $X$  can be for example  $p_T$ . Those matrices are equivalent  $f(true) \cdot P(reco|true)$ . Then, events in each bin of spectra we want do correct are redistributed using normalized slices in given value of  $reco$  of the matrix, where normalization is done by the division by  $g(reco)$  in Formula 6.3. Matrix is in next step updated (this is equivalent to multiplying it by  $f^r(true)/f(true)$ ) and whole process is repeated.

## 6.2 Correction to $\frac{1}{N_{ev}} \frac{dN_{ev}}{dn_{ch}}$

As was mentioned before, this distribution describes number of events per number of charged particles. Furthermore, its integral gives number of events in the studied phase-space, which is needed for the  $1/N_{ev}$  factor in the other distributions.

First, the spectrum is corrected by the event weight. Then the Bayesian unfolding, discussed in previous section, is applied in order to compensate for migration between bins. What is the main source of this migration? Since the track efficiency is only around 80%, event with e.g. 5 tracks will be on average reconstructed as event with 4 tracks. This results in shift of events towards lower multiplicities.

The migration matrix used is a 2D histogram, where on one axis there is number of tracks after selection and on the second axis a number of primary particles within the kinematic region.

Obviously, some events may loose so many tracks, that they are reconstructed with not enough tracks to pass the selection at all, migrating out of the defined phase-space. Correction of this is made easier by the fact that tracking efficiency as function of number of selected tracks is constant within few percent and therefore we can correct with mean tracking efficiency  $\varepsilon_{trk}$ .

In our case we require  $n_{ch} \geq 1$ , event therefore migrates out of the phase-space if it loses all tracks. Probability of that is easily  $(1 - \varepsilon_{trk})^{n_{ch}}$  and the weight for each  $n_{ch}$  takes following form:

$$1/(1 - (1 - \varepsilon_{trk})^{n_{ch}}). \quad (6.4)$$

Influence of corrections for lower values of  $n_{ch}$  is in Figure 6.1. For higher values is not the effect that significant. Aside from the  $N_{ev}$ , important output of this procedure is the final migration matrix, which is used to unfold the  $\langle p_T \rangle$  vs.  $n_{ch}$ .

## 6.3 Correction to mean $p_T$ vs $n_{ch}$

Mean  $p_T$  is computed by dividing two histograms. First is  $\sum p_T$  vs  $n_{ch}$ , meaning that for every tracks corresponding  $n_{ch}$  bin is filled by a value of  $p_T$ . Second histogram is similar, but is filled with 1, giving total number of tracks per each bin  $\sum trk$ . Ratio of those two gives uncorrected (raw) distribution of  $\langle p_T \rangle$  vs.  $n_{ch}$ .

In second step, each track is weighted with event and track weight. The tracking efficiency has small effect on final distributions, however it allows comparison of the  $\sum p_T$  and  $\sum trk$  between track and

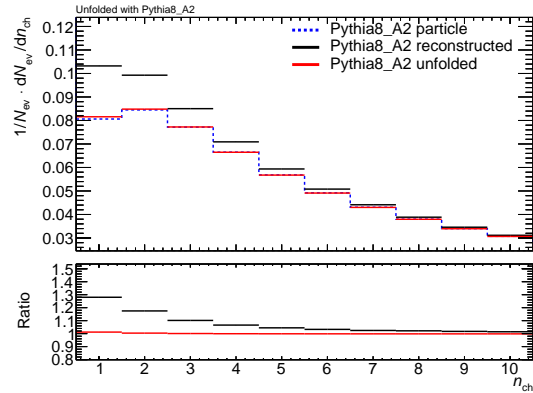


Figure 6.1: Effects of corrections on the distribution of events vs.  $n_{ch}$ . Produced for Pythia 8 A2 unfolded also by Pythia 8 A2. Courtesy to Oldřich Kepka.

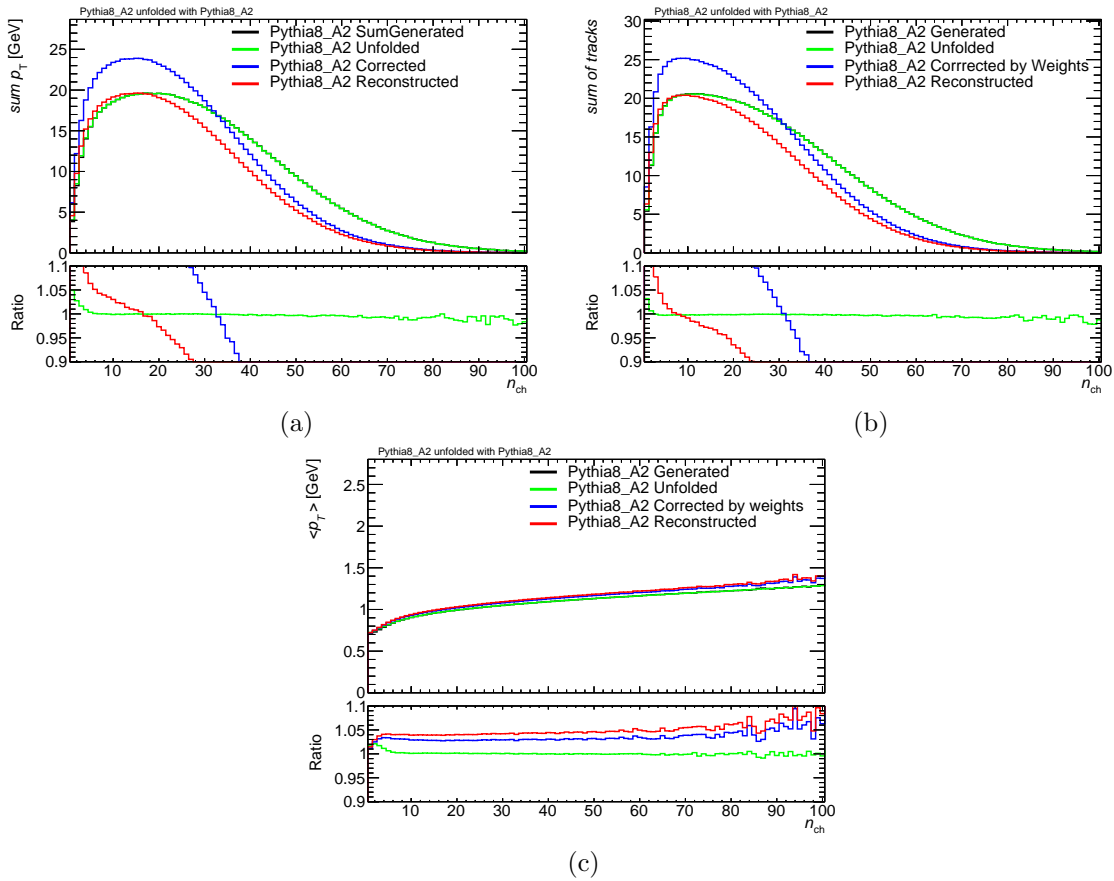


Figure 6.2: Effects of various steps of corrections on a) sum of  $p_T$  and b) sum of tracks distributions. (c) is mean  $p_T$ , obtained by division of sum of  $p_T$  by sum of tracks. Generated refers to spectrum on particle level. Produced from Pythia 8 A2 sample unfolded also by Pythia 8 A2 sample.

particle level. This is useful when searching for origins of non-closure (difference between corrected and generated spectrum). Whole procedure is finished by using Bayesian unfolding to correct for migration. It uses the final matrix coming from iterative process for  $\frac{1}{N_{ev}} \frac{dN_{ev}}{dn_{ch}}$  and is again used separately on both distributions.

Impact of various steps can be seen in Figure 6.2. Correction by track and event weight shifts the spectrum, adding tracks which were not reconstructed. Resulting distribution is shifted in comparison to the generated spectrum toward the lower multiplicities, as it was in case of  $\frac{1}{N_{ev}} \frac{dN_{ev}}{dn_{ch}}$ . Finally, unfolding moves those tracks to get the final distribution, which is in good agreement with the generated spectrum. Small difference in lower  $n_{ch}$  is there because the migration matrix was designed for the event distribution and not  $\sum p_T$  or  $\sum trk$ .

## 6.4 Corrections to $\frac{1}{N_{ev}} \frac{dN_{ch}}{d\eta}$ and $\frac{1}{N_{ev}} \frac{1}{2\pi p_T} \frac{d^2 N_{ch}}{d\eta dp_T}$ distributions

As was mentioned earlier, the normalisation factor  $N_{ev}$  for those distributions is taken from the final results of the  $n_{ch}$  spectrum.

Since resolution in  $\eta$  is fairly high, migration between bins is not a problem and unfolding procedure is not applied for the  $\eta$  distribution. Only event and track weight is used to get final distribution. Effect of this correction can be seen in Figure 6.3. Difference between particle level and corrected spectrum is smaller than 1%.

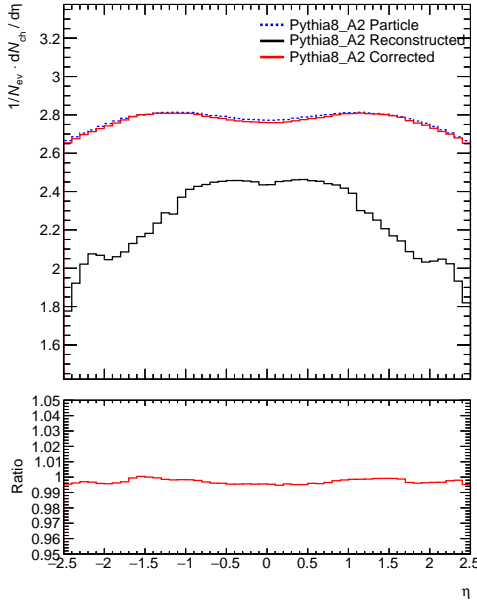


Figure 6.3: Effects of corrections on the  $\eta$  distribution. Produced for Pythia 8 A2 generator.

Transverse momentum distribution is corrected with event and track weights. Unfolding procedure similar to that used in  $n_{ch}$  corrections is then applied. Migration matrix used has on one axis  $p_T$  of tracks with right selection and on the second axis  $p_T$  of primary particles within the right kinematic region. Main source of migration are mis-measured track, low  $p_T$  particles reconstructed as high  $p_T$  tracks, which affects the  $p_T$  distribution for higher values.

As can be seen in Figure 6.4, weight correction gives already really good results, comparable to generated spectrum up to cca 10 GeV, then it slowly diverges. Unfolding corrects this effect and the difference is smaller than 5% for 100 GeV.

Effect of individual iterations of the unfolding is in Figure 6.5. The convergence is quicker when spectrum is unfolded by the same model, but for example in case of the EPOS unfolded by the Pythia 8 A2 it is obvious, that after four iteration is further effect negligible. Difference between generated and reconstructed spectrum is mainly due to large statistical uncertainties. Since  $p_T$  spectrum falls quickly, there are only few tracks in high  $p_T$  in both the spectrum and the matrix.

This problem is solved by usage of a single particle generators, which populate whole  $p_T$  region uniformly. When unfolding data, all generators are combined, ensuring good statistics. Consequently, combined model has worse description of data, mainly due to the single particle generators, requiring more iterations to convergence.

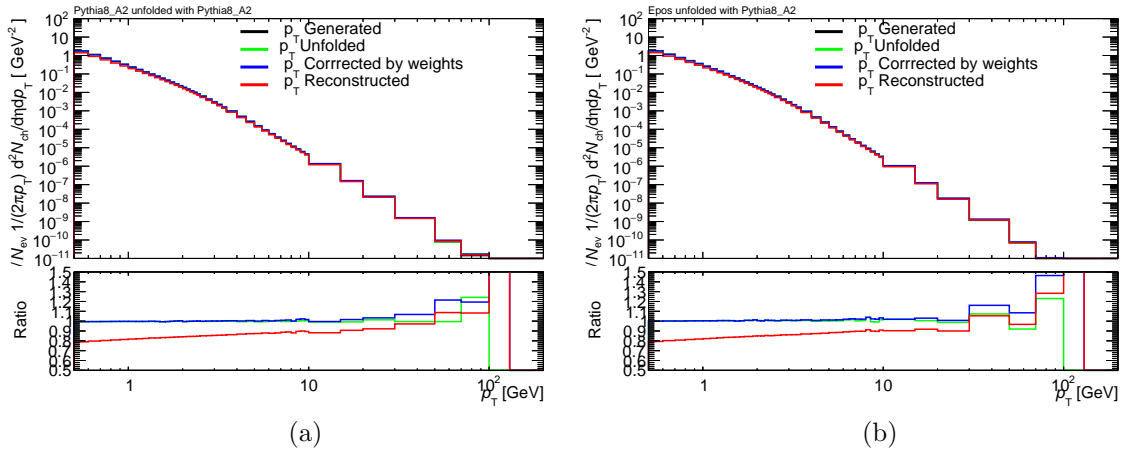


Figure 6.4: Effects of various steps of corrections on  $p_T$  distributions. Produced for (a) Pythia8 A2 and (b) EPOS unfolded using Pythia A2.

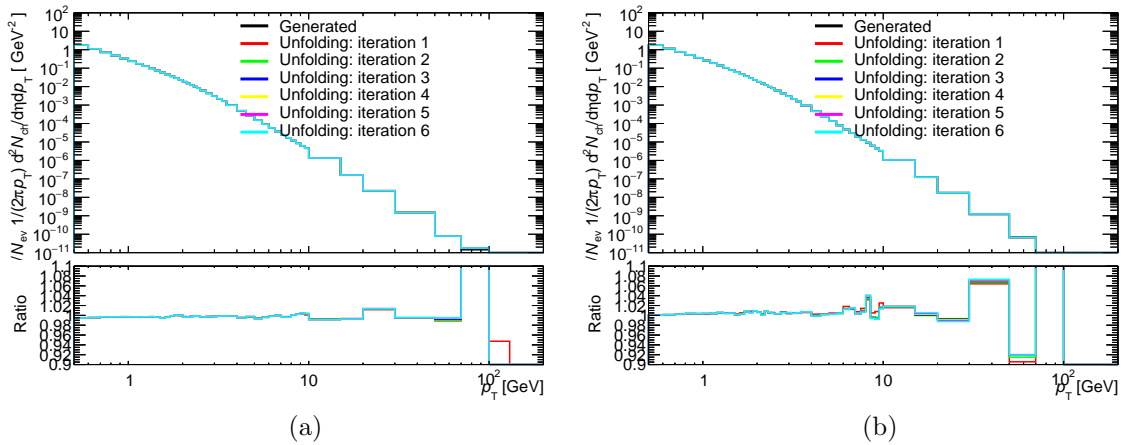


Figure 6.5: Effect of iterative unfolding on  $p_T$  distribution, compared to the generated distribution. Six iterations are shown, demonstrating convergence of the unfolding. Produced for (a) Pythia8 A2 and (b) EPOS unfolded using Pythia A2.

# Chapter 7

## Analysis of 13 TeV data

In time of writing of this thesis, an official analysis report was not yet published. However, a draft of the paper [7] and supporting note [6] should cover all important aspects and in many cases offer more detailed information about the analysis and its results.

My work on this analysis focused mainly on two parts. First part was to create framework, which will select events and tracks and fill important histograms. It had to be able to apply corrections and process both reconstructed and particle spectra. Second part was to prepare program, which produces efficiencies, fractions and weights, which are filled back to the analysis framework. It also had to be able to further correct spectra by for example application of unfolding procedure and calculate total errors of the distributions.

### 7.1 13 TeV data

Sample used in our case had an integrated luminosity of  $169\mu\text{b}^{-1}$ [6] and was taken from 9<sup>th</sup> to 13<sup>th</sup> June 2015. From this sample, two runs<sup>1</sup> were chosen for our analysis: run 267358 and 267359. First run had probability of additional interaction in same bunch crossing equal to 0.3%, which is lower than expected, the second had more reasonable probability 0.7%.

Luminosity blocks of both runs were further selected to discard problematic events, when for example some part of detector did not function properly. From around 20 million events taken in these runs, only approximately 10.8 million passed the selection on MBTS<sup>2</sup> trigger and luminosity blocks. After the event selection, this number was further reduced to 8870790 events.

### 7.2 Re-weighting of the Monte Carlo

One of the properties of vertex is its position. Since for data distribution of vertices is not known in advance and sometimes it varies significantly from the generated spectrum, Monte Carlo must be adjusted in order to compensate for this. Otherwise, comparison of data and Monte Carlo would be impossible. Difference between data and Pythia 8 A2 before any changes can be seen for the  $z$  coordinate in Figure 7.1a.

Correction of this discrepancy is done by re-weighting of the Monte Carlo, where the  $d$  coordinate is not weighted since it is modelled with reasonable accuracy. Weight is defined as ratio of the  $z$  coordinates of data and of Monte Carlo scaled to data. It can be found in Figure 7.1b. Each event and each track of that event is weighted by value corresponding to  $z$  of the Monte Carlo. Now it is possible

---

<sup>1</sup>Data taken by ATLAS are divided into runs, which are further divided into luminosity blocks. Luminosity block covers approximately 2 minute intervals and consists of individual events.

<sup>2</sup>More precisely trigger HLT\_noalg\_MBTS\_1.

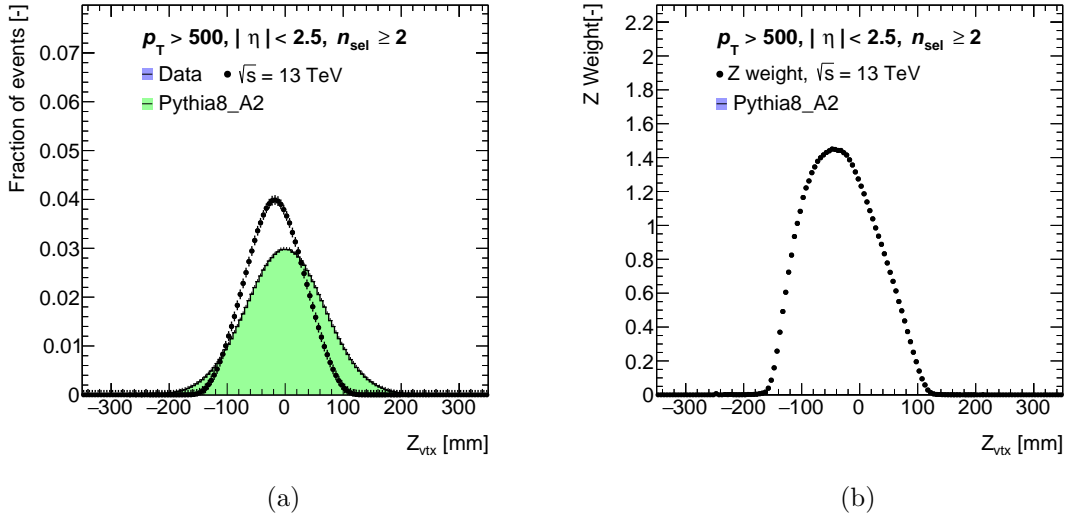


Figure 7.1: (a) shows distributions of vertices as function of  $z$  for data and Pythia 8 A2, where the Pythia 8 A2 is scaled to data, and (b) shows corresponding  $z$ -weight.

to compare data and models. Figure 2.4 shown in chapter about the detector is for re-weighted Monte Carlo and shows good agreement between data and the generators for number of Pixel and SCT hits.

### 7.3 Raw distributions

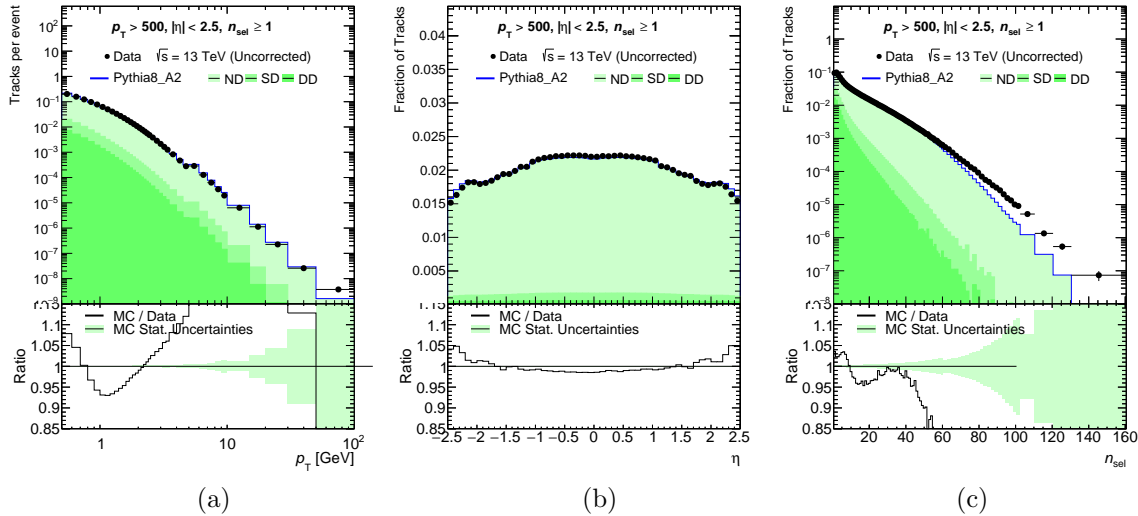


Figure 7.2: Raw distribution of tracks per (a)  $p_T$ , (b)  $\eta$  and (c) distribution of events per number of charged particle for data and Pythia 8 A2 with their ratio, normalized to 1.

Uncorrected spectra are simplest to produce and are therefore ideal to estimate how accurately the generators describe physics of the collision. In case of this analysis, first results were optimistic. Plots in Figure 7.2 show comparison of data and Pythia 8 A2 simulation, where both are scaled such that integral of the histogram gives 1, enabling to compare shapes and thus seeing how good is the detector

simulation. It shows surprisingly good correspondence between measured data and MC, mainly for low  $p_T$  a  $n_{ch}$  and whole  $\eta$  region. This means that we are able to model quite precisely shape of the distribution, mainly in  $\eta$ . More realistic view is in Figure 7.6 in Appendix A, where the distributions are normalized by number of events. Here it is obvious that there is more tracks in data than in simulation, though only by approximately 5%.

Precise image of quality of the simulation can be only acquired through study of corrected spectra. The reconstructed spectra are corrected by procedures described in previous chapter, in same way Monte Carlo was corrected. After that, errors must be estimated. Short overview of systematic and statistical errors is given in following section.

## 7.4 Systematic and statistical errors

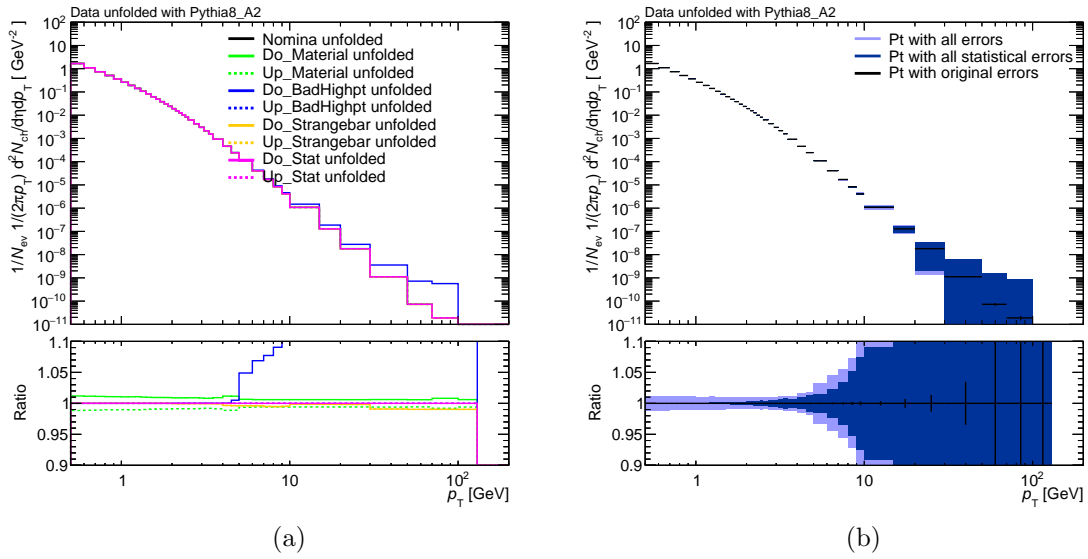


Figure 7.3: (a) Comparison of systematic distributions for  $p_T$ , where all have up and down variation, which is then for each systematic added up and divided by two. (b) shows the statistical and systematic errors for the  $p_T$ .

Proper description of the systematics errors would require several chapters and is beyond scope of this thesis. Here, only basic idea and some examples are introduced. Thorough description can be found in the support note of the analysis [6].

Systematic errors are done for e.g. material, because precise model of the detector is impossible, or for secondary particles, since various models predict different distributions. They are propagated in several steps.

In the first step, distributions of interest are obtained with modified weights. Modification depends on the type of the systematic studied, some details can be again found in the support note [6]. Spectra affected by the systematic variation are then corrected by unfolding in same way as was the nominal spectrum. Thus, several distributions are acquired, examples of them can be found in Figure 7.3a for case of the  $p_T$  distribution.

Systematic error is then calculated by summing contribution, or more precisely the difference between nominal and given systematic, from all systematic sources. Thus, systematic errors is acquired and it can be combined with statistical error.

Statistical error comes directly data and from the unfolding. While the former is calculated automatically, the latter requires more complicated approach. In our case, the statistical error is estimated

by modifying each bin of migration matrix by poisson distribution and then performing normal unfolding. This procedure is repeated about 100 times and results in that number of unfolded spectra, which slightly vary from the nominal value. The statistical error of unfolding is then estimated from the variance of values in each bin.

Statistical error with and without contribution from unfolding together with the final error can be seen in Figure 7.3b.

## 7.5 Final results

After application of all corrections, data can be finally compared to various models. Densities of particles versus  $p_T$  and  $\eta$  are in Figure 7.4, distribution of events versus  $n_{ch}$  and mean  $p_T$  versus  $n_{ch}$  are in Figure 7.5.

The  $p_T$  distribution is best described by the EPOS, which agrees with data up to roughly 5 GeV. The Pythia 8 A2 tune matches within 10% for this region, while the Monash and QGSJET predict more particles and different structure. The Herwig++ gives the worst description, it has more than 20% even in  $p_T$  as low as 300 MeV.

As in previous case, the EPOS again provides the best description of the data in the  $\eta$  distribution, it doesn't differ by more than 10% in most of the spectrum. Both Pythia tunes describe the shape quite well, though Monash is approximately 5% higher and A2 5% lower. Also QGSJET gives good description of shape but predicts much more particles. The Herwig++ again fails to describe the shape and values.

Event distribution vs.  $n_{ch}$  is quite well described by the EPOS, QGPJET and both Pythia tunes for  $n_{ch} < 40$ , while HERWIG shows much more events in lowest bins and lower values for most of the spectra. After the  $n_{ch} = 40$  all generators diverge from the data, mainly QGSJET shows much more events for multiplicity greater than 60.

Finally, mean  $p_T$  is modelled really well by most of the generators, mainly by the Pythia 8 Monash tune. The Pythia 8 A2 predicts steeper rise of the mean  $p_T$ , but only by about 10% (aside from the last bin, where there is a low statistics and the spectra and therefore the results are not that precise) and HERWIG++ has smaller value over almost whole spectrum, though with right shape. Only QGSJET fails to describe the spectrum, showing almost constant dependence of mean  $p_T$  on number of charged particles.

From the corrected  $n_{ch}$  distribution it is determined, that number of selected events after correction is 9161732, about 3% more than number of measured events.

For events with at least one charge particle with  $p_T > 500$  MeV and  $|\eta| < 2.5$ , average particle density around  $\eta = 0$  is  $2.876 \pm 0.001922(stat.) \pm 0.03526(syst.)$ , as can be found out from the  $\eta$  distribution, performing an average in the range  $|\eta| < 0.2$

Overall most of the generators describe the data quite well. This was not the case for the first run of the LHC, where the differences were much bigger. It shows that tuning from 7 TeV data has good descriptive power for current energies, though it is still necessary to improve the models.

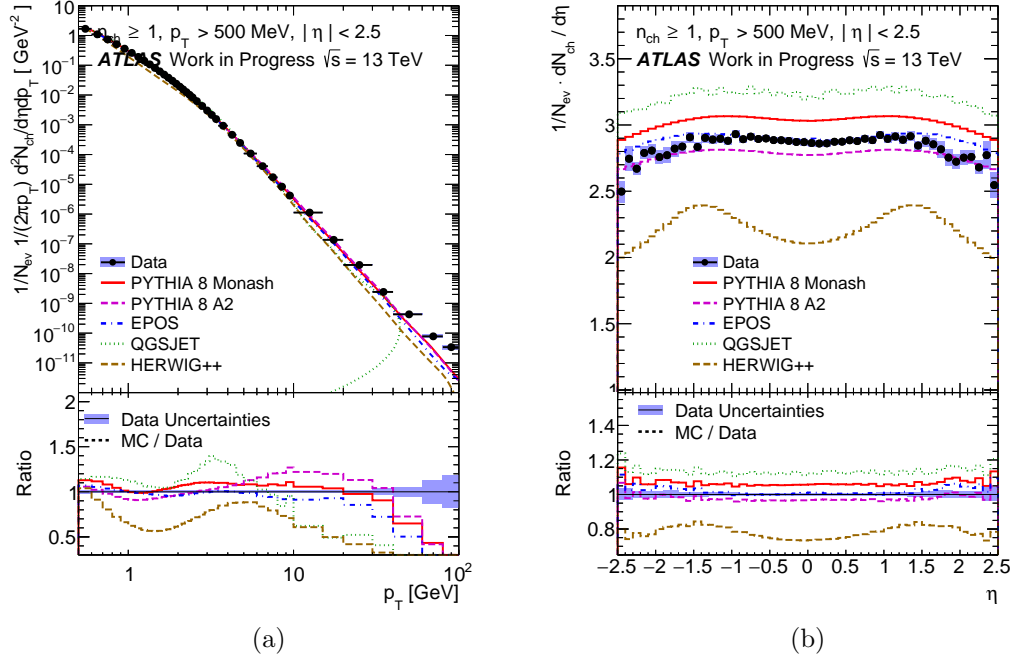


Figure 7.4: Comparison of corrected data and various Monte Carlo generator, (a) shows distribution  $\frac{1}{N_{ev}} \frac{1}{2\pi p_T} \frac{d^2 N_{ch}}{d\eta dp_T}$ , (b) shows distribution  $\frac{1}{N_{ev}} \frac{dN_{ch}}{d\eta}$ .

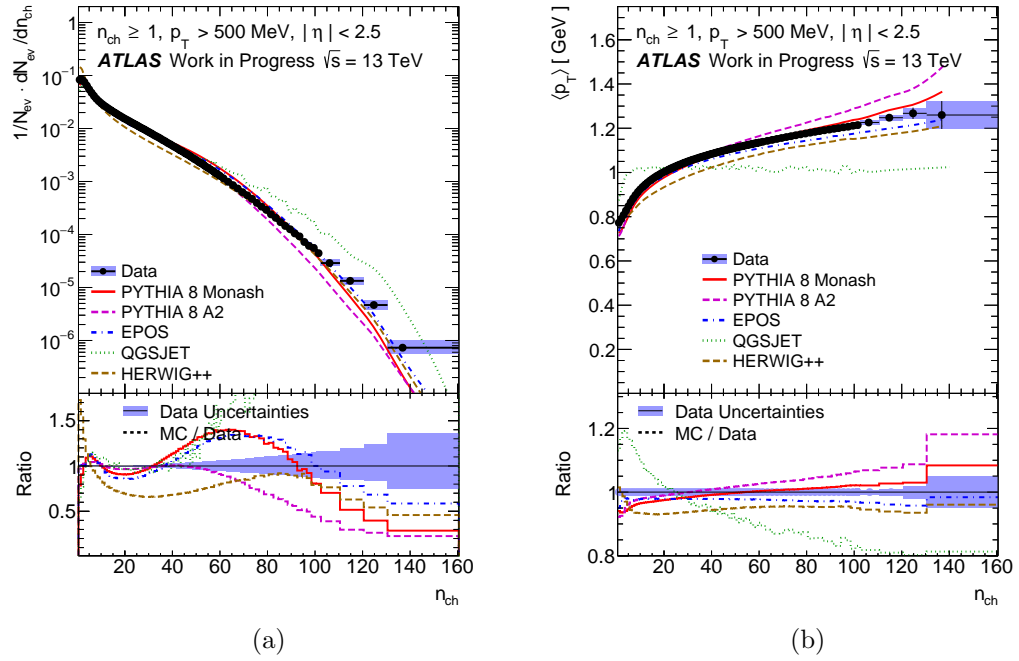


Figure 7.5: Comparison of corrected data and various Monte Carlo generator, (a) shows distribution  $\frac{1}{N_{ev}} \frac{dN_{ev}}{dn_{ch}}$ , (b) shows distribution  $\langle p_T \rangle$  vs  $n_{ch}$ .

# Summary

Main focus of this thesis was to describe measurement of charged particles at the LHC for  $\sqrt{s} = 13$  TeV. It is inclusive measurement necessary for tuning of generators, which is important for analyses of processes with low cross-section. At first, Chapter 1 gives short overview of QCD and simulation of the collision. Also Monte Carlo generators used throughout the analysis are introduced. Next, attributes of the ATLAS detector important to the measurement were described in Chapter 2, mainly Inner Detector and MBTS trigger.

Further, tracking and vertexing was introduced in Chapter 3, focusing on techniques used on the ATLAS: inside-out and outside-in tracking algorithm. Selections and studied regions were defined and their purpose explained throughout the Chapter 4, together with background description and correction by weights. Chapter 5 reviewed my work on efficiencies for events and tracks, followed by fractions of secondary and migrating tracks. Efficiencies and fractions are further used to correct the reconstructed spectrum. Correction procedure, mainly Bayesian unfolding, was explained in Chapter 6, followed by my results of the procedure for the  $p_T$  and  $\eta$  density and for the  $\langle p_T \rangle$  vs.  $n_{ch}$  distribution.

Finally, Chapter 7 presented the  $\sqrt{s} = 13$  TeV data and rest of methods used to get final results. Figures of uncorrected and final results were then shown and compared with number of Monte Carlo generators: Pythia 8 (A2 and Monash tunes), EPOS, Herwig++ and QGSJET. EPOS and both Pythia 8 tunes are in relatively good agreement with data.

# Appendix A - Additional results

Uncorrected spectra scaled by number of events are in Figure 7.6. As was mentioned in results, it shows that Pythia 8 A2 predicts less particles than we see in data. We also see much more events for high number of selected tracks, as can be seen in (c) of same figure. This difference is already more than 10% for 50 selected particles.

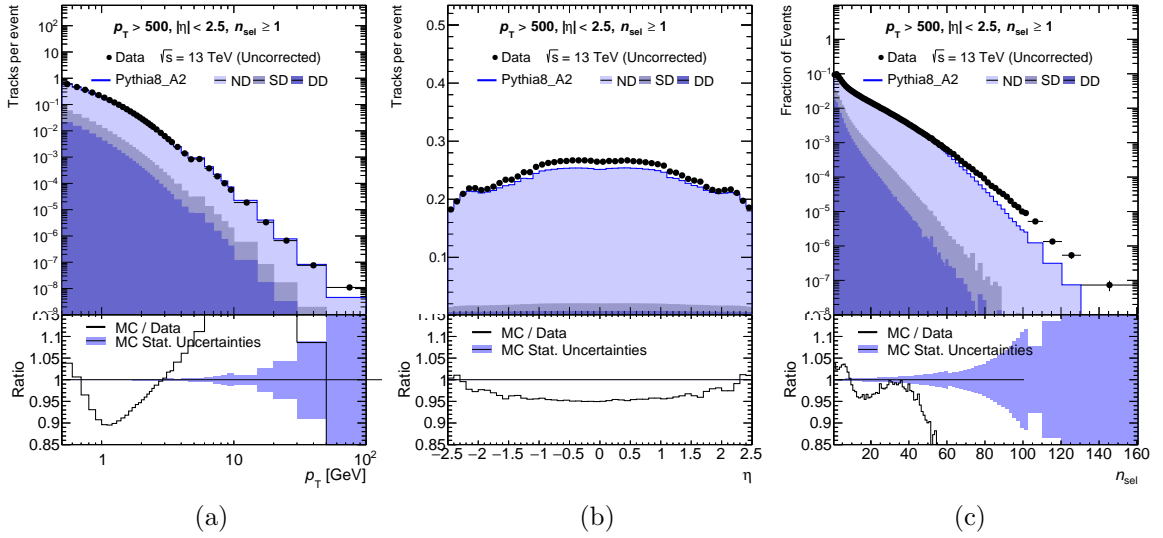


Figure 7.6: Raw distribution of tracks per  $p_T, \eta$  and raw distribution of events per number of charged particle for data and Pythia 8 A2 with their ratio. All distributions are normalized by number of events, giving number of tracks per event.

# Bibliography

- [1] G. Aad *et al.* [ATLAS Collaboration], “Charged-particle multiplicities in pp interactions measured with the ATLAS detector at the LHC,” *New J. Phys.* **13** (2011) 053033 [arXiv:1012.5104 [hep-ex]].
- [2] P. Skands, “Introduction to QCD,” [arXiv:1207.2389 [hep-ph]].
- [3] T. Sjostrand, “Monte Carlo Tools,” (2009) [arXiv:0911.5286 [hep-ph]].
- [4] A. Buckley, J. Butterworth, S. Gieseke, D. Grellscheid, S. Hoche, H. Hoeth, F. Krauss and L. Lonnblad *et al.*, “General-purpose event generators for LHC physics,” *Phys. Rept.* **504** (2011) 145 [arXiv:1101.2599 [hep-ph]].
- [5] R. Placakyte, “Parton Distribution Functions,” [arXiv:1111.5452 [hep-ph]].
- [6] Morley, Anthony Keith and Kuhl, Thorsten “Supporting note for the Minimum Bias publication: Charge particle multiplicity in pp interactions at 13 TeV measured with the ATLAS detector,” Supporting note, CERN, Geneva, (2015) ATL-COM-PHYS-2015-313.
- [7] Nurse, Emily and Kuhl, Thorsten and Morley, Anthony Keith “Charged-particle multiplicities in  $\sqrt{s}=13$  TeV pp interactions measured with the ATLAS detector at the LHC,” Draft of paper, CERN, Geneva, (2015) ATL-COM-PHYS-2015-346.
- [8] Stephen Myers, “The large hadron collider 2008–2013,” *Int. J. Mod. Phys. A*, **28** (2013) 1330035 [DOI: 10.1142/S0217751X13300354].
- [9] G. Aad *et al.* [ATLAS Collaboration], “Studies of the performance of the ATLAS detector using cosmic-ray muons,” *Eur. Phys. J. C* **71** (2011) 1593 [arXiv:1011.6665 [physics.ins-det]].
- [10] G. Aad *et al.* [ATLAS Collaboration], “The ATLAS Experiment at the CERN Large Hadron Collider,” *JINST* **3** (2008) S08003.
- [11] A. Siidoti, “Minimum Bias Trigger Scintillators in ATLAS Run II,” *JINST* **9** (2014) C10020.
- [12] M. Limper, “Track and Vertex Reconstruction in the ATLAS Inner Detector,” Amsterdam, Netherlands: Eigenverl. (2009).
- [13] L. de Nooij, “The  $\Phi(1020)$ -meson production cross section measured with the ATLAS detector at  $\sqrt{s} = 7$  TeV,” CERN-THESIS-2014-035.
- [14] Giordani, M, “Overview of the ATLAS Insertable B-Layer (IBL) Project,” ATL-INDET-SLIDE-2012-428.
- [15] T. Cornelissen, M. Elsing, S. Fleischmann, W. Liebig, E. Moyses and A. Salzburger, “Concepts, Design and Implementation of the ATLAS New Tracking (NEWT),” **25** (2007) ATL-SOFT-PUB-2007-007, ATL-COM-SOFT-2007-002.

- [16] Holger Schulz, Michael Leyton, Heiko Lacker “Measurement of hadron collider event shapes in  $Z \rightarrow l^+l^-$  events at  $\sqrt{s} = 7$  TeV with ATLAS,” Technical Report, CERN, Geneva, (2014) ATL-COM-PHYS-2014-285.
- [17] G. Aad et al. [ATLAS Collaboration], “Track Reconstruction Efficiency in  $\sqrt{s}=7$  TeV Data for Tracks with  $p_T > 100$  MeV,” Technical Report, CERN, Geneva, (2010) ATL-COM-PHYS-2010-682.
- [18] G. Aad *et al.* [ATLAS Collaboration], “Charged-particle multiplicities in pp interactions at  $\sqrt{s} = 7$  TeV and 900 GeV measured from  $p_T > 100$  MeV: Supporting the MinBias 2nd Publication,” Technical Report, CERN, Geneva, (2010) ATL-COM-PHYS-2010-880.
- [19] Aaron Armbruster, Kevin Kröniger, Bogdan Malaescu, Francesco Spano, “Practical considerations for unfolding,” Technical Report, CERN, Geneva, (2014) ATL-COM-PHYS-2014-277.